Surface plasmon polariton propagation in straight and tailored waveguides

Samenstelling van de promotiecommissie:

prof. dr. L. Kuipers (promotor)	Universiteit Twente
prof. dr. J. L. Herek	Universiteit Twente
prof. dr. N. F. van Hulst	ICFO - Institut de Ciències Fotòniques
prof. dr. F. J. García de Abajo	Instituto de Optica - CSIC
prof. dr. F. Mugele	Universiteit Twente
dr. M. P. van Exter	Universiteit Leiden

The work described in this thesis is part of the research program of the
"Stichting Fundamenteel Onderzoek der Materie" (FOM), which is financially
supported by the
"Nederlandse Organisatie voor Wetenschappelijk Onderzoek" (NWO).

This work was carried out at:
NanoOptics Group,
FOM-Institute for Atomic and Molecular Physics (AMOLF)
Kruislaan 407, 1098 SJ Amsterdam, The Netherlands,
where a limited number of copies of this thesis is available.

Cover design: Iliya Cerjak
ISBN: 978-90-77209-16-5
Printed by: Ponsen & Looijen B.V., The Netherlands.

Surface plasmon polariton propagation in straight and tailored waveguides

Proefschrift

ter verkrijging van
de graad van doctor aan de Universiteit Twente,
op gezag van de rector magnificus,
prof. dr. W. H. M. Zijm,
volgens besluit van het College voor Promoties
in het openbaar te verdedigen
op vrijdag 29 juni 2007 om 16:45 uur

door

Marijn Sandtke

geboren op 18 maart 1979
te Delft

Dit proefschrift is goedgekeurd door:
prof. dr. L. (Kobus) Kuipers

Contents

Chapter 1

Introduction

1.1 The need for a new technology

Since the introduction of devices like the personal computer and the mobile phone, silicon technology is no longer an *important* technology, it is a *vital* technology. Western society can no longer exist without silicon technology. Both consumers and industry require ever smaller and faster PC's and chips, and therefore the technology inside has to shrink continually. The chip industry has in fact sets its own milestones by trying to keep up with Moore's law. Intel co-founder Gordon Moore stated in 1965 that manufacturers would double the number of transistors on a chip every 18 months [1]. Although this roadmap is diligently followed, around 2014 the technology will face what has been termed the ultimate "red brick wall": a key feature called the gate oxide will become so thin that it effectively disappears [2].

Meanwhile, pushing the size limits raises additional problems. For instance chip heating is not negligible anymore. Miniaturization also pays its toll at interconnects and long distance (chip scale) information transportation [3], as the bandwidth of the current technologies starts to approach its limits. Thus, as the drive for both smaller and faster chips continues, solving the upcoming limits asks for unconventional solutions.

Part of the upcoming problems can be solved by optics, or photonics. Optical interconnects such as optical fibers are able to carry digital data with a bandwidth > 1000 times higher than that of copper wire electronic interconnects [4]. For this reason internet traffic between Europe and the US runs through optical fibers. Also in clock distribution and intra chip global signaling optical interconnects are being explored to replace the Cu wires [3]. Equally important is the benefit that optical fibers do not heat up while transporting information.

A lot of the "high speed" promise is lost in converting the optical signals to the electrical signals that a current chip uses. This "loss in speed" also arises in large scale global telecommunication. Routers switch light by converting optical pulses into an electronic signal, switch electronically and converting the resulting electronic signal back into optical pulses. Large improvements can be made at this point. Another drawback of using optics is that an optical fiber has a much larger diameter compared to Cu electrical interconnects. The diffraction limit sets boundaries for miniaturizing optical signal processing. This can be solved for instance by using photonic crystals [5], but an alternative is to use surface plasmon polaritons (SPPs). An attractive aspects of SPPs is that they concentrate and channel light using subwavelength structures. This could lead to miniaturized photonic circuits with length scales much smaller than the diffraction limit [6].

Moreover, SPPs are able to integrate optics and electronics as they can use the same interconnects [7].

1.2 Surface plasmon polaritons

SPPs are propagating solutions of Maxwell's equations at the interface between a dielectric and a metal, which are bound to that interface [6, 8]. They are the resonant interaction between a light wave and oscillations of the free electrons at the metal interface and have an evanescent tail into both the metal and the dielectric.

The dispersion of SPPs on a smooth metal surface is given by [8]:

$$k_x = \frac{\omega}{c}\left(\frac{\epsilon_m \epsilon_d}{\epsilon_m + \epsilon_d}\right)^{\frac{1}{2}}, \tag{1.1}$$

here k_x is the SPP wavevector, c the speed of light in vacuum, ω the optical frequency of the SPP and ϵ_m and ϵ_d are the dielectric constant of the metal and the dielectric, respectively. The x-direction is the direction of propagation as also defined in figure 1.1. The SPP propagation length δ_x is given by:

$$\delta_x = \frac{1}{2Im(k_x)}, \tag{1.2}$$

with $Im(k_x)$ the imaginary part of k_x. Typical values for δ_x are in the order of 100 μm for Ag as the supporting metal and a wavelength in air of 1.5 μm.

The imaginary wavevector perpendicular to the metal dielectric interface, k_z, determines the exponential decay of the evanescent field of the SPP E-field in the z-direction, E_z,:

$$E_z \sim exp(-|k_z|z), \tag{1.3}$$

with:

$$|k_{z(m,d)}| = \left|\left[\epsilon_{m,d}\left(\frac{\omega}{c}\right)^2 - k_x^2\right]^{1/2}\right|. \tag{1.4}$$

This means that the skin depth $\delta_{z(m,d)}$ of the SPP is given by:

$$\delta_{z(m,d)} = \frac{1}{2Im(k_z)}. \tag{1.5}$$

Typical values for $\delta_{z(m,d)}$, with Ag as supporting metal and a wavelength in air of 1.5 μm, in the dielectric and metal are in the order of 100 nm and 10 nm, respectively. Figure 1.1 shows a cartoon of the amplitude of a SPP E-field, and its evanescent tail into the metal and dielectric.

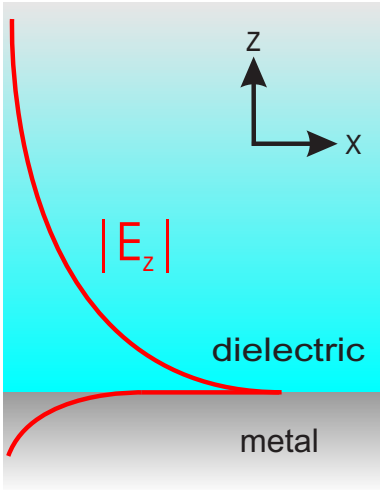

Figure 1.1: *Cartoon of the SPP's E-field. It is concentrated at the interface between a metal and a dielectric, and has an evanescent tail into both media.*

In order to excite SPPs with photons, the wavevector of the SPPs has to match the wavevector of the photons. Since $Re(\epsilon_m) < 0$ for all frequencies below the bulk plasmon frequency, and $|Re(\epsilon_m)| > \epsilon_d$, it is clear that $k_x > \frac{\omega}{c}\sqrt{\epsilon_d}$. Therefore, SPPs cannot be excited directly with photons incident from the dielectric. Three routes for SPP momentum matching exist: using a subwavelength scatterer, grating coupling or attenuated total reflection (ATR). In the first case, a subwavelength point or line defect, provides the necessary uncertainty in k-space to match the wavevectors [8]. In the case of grating coupling, one or multiple grating constants can be added (or subtracted) to the photon wavevector to match the wavevector of the SPP [8].

For ATR, also called the Kretschmann-Raether configuration, the incident light propagates through a different dielectric medium than the dielectric that will support the SPP [9]. This dielectric should have a dielectric constant $\epsilon_{d2} > \epsilon_d$. In this thesis a BK7-glass prism is used to excite SPPs at the interface between air and Au. The light propagating through the prism is incident on the metal-glass interface, with a wavevector component parallel to the metal surface, $k_{x,photon}$, which is:

$$k_{x,photon} = \sqrt{\epsilon_{d2}}\frac{\omega}{c}sin\theta, \tag{1.6}$$

where θ is the angle between the surface normal and incoming light. At the angle for total internal reflection at the glass-metal interface and larger angles, total internal reflection occurs. An evanescent tail of the incident light will penetrate the metal and for sufficiently thin metal films the tail will reach the metal-air interface

and can excite SPPs. Matching between the wavevector of the incoming photons and the SPP wavevector at the metal-air interface can now be achieved by tuning θ. With this method coupling efficiencies up to 90% are achievable.

The fact that the wavevector of a SPP is larger than that of light in air with the same frequency has a huge advantage for applications: it allows for propagation and manipulation on a length scale smaller than the diffraction limit as was mentioned before [10, 11]. Moreover, SPPs are being explored for applications in data storage [12], improving conventional microscopy [13] and solar cells [14]. In 1990 the company Biacore, brought a commercial instrument on the market that detects biomolecular interactions, using SPPs. These detectors make use of the fact that SPPs are extremely sensitive to changes in the dielectric constant at the surface. Small changes in ϵ_d at the surface, because of the presence of biomarkers, will change k_x and therefore change the wavevector matching during ATR. This change in coupling efficiency can be detected very accurately [15].

If we want to apply SPP in telecommunication, or enhance the sensitivity of excising sensors, lots of fundamental questions about SPP behavior on subwavelength scales need to be answered. For instance, how do SPPs behave in nm size switches, couplers or guides? How much is the SPP dispersion changed in such structures? Can SPPs be slowed down as will be necessary in a SPP router, or to enhance the sensor sensitivity [16]? Once the basic properties of the SPPs are well understood, scientists can start with the next step: implementing SPP devices into (existing) applications.

1.3 SPP detection

SPP properties at small length scales are hard to model. Therefore, an instrument is desired to study SPP characteristics like propagation length, group and phase velocity, and its dispersion. To capture the intriguing nature of SPPs in metal nanostructures, that are also relevant to applications, the instrument needs to be able to measure on subwavelength scales. Also, the instrument requires phase-sensitivity to gain maximum insight.

Various methods exist to study SPPs in the far-field, of which detecting the leakage radiation [17] is the oldest and most widely used technique. Drawback of this technique is that one measures the scattered field, which requires defects in the structure. Also the scattered photons are detected with a conventional (confocal) microscope, that is limited by diffraction. More recent, fluorescent probes such as day molecules [18] and Er^{3+} ions [19] are proposed. These techniques make it

possible to image bound modes, but are still bound the diffraction limit. A way to beat the diffraction limit is to combine interferometric time-resolved two-photon photoemission (ITR-2PP) and photoelectron emission microscopy (PEEM) [20]. With this technique SPP measurements with < 10 fs temporal and 60 nm spatial resolution are presented [21]. Drawback of PEEM is that it requires an ultra high vacuum.

1.3.1 Near-field microscopy

Near-field microscopy [22, 23] or a photon scanning tunnelling microscope (PSTM), is another technique that can beat the diffraction limit. Because of its ability to detect evanescent fields on a subwavelength scale, a PSTM is ideal for measuring SPPs [24, 25]. For photonic nanostructures it has been shown that a PSTM can be adapted to obtain phase-sensitivity and to be ultrafast on the fs time scale [26–32]. A PSTM uses a near-field probe (an optical fiber with a nm scale aperture) instead of a lens. As the probe is brought within a few nanometer of the metal surface, part of the evanescent tail of the SPP is able to couple to the probe, and is subsequently detected in the far-field. The size and geometry of the probe determine the resolution, instead of diffraction, and subwavelength resolution can be obtained. Multiple studies using a PSTM on (guided) SPPs are reported in literature over the last couple of years [24, 25, 33–37]. However, with one notable exception [37], none of these studies show the phase of the SPP, or time-resolved information.

1.4 Results presented in this thesis

In this thesis time-sensitive and phase-resolved, near-field measurements on propagating SPP wavepackets are presented. Measurements were performed on both straight SPP guides and a plasmonic crystal. We show it is possible to measure the phase and group velocity of guided SPPs, and that the group velocity can be modified by introducing a SPP Bragg grating along the guide.

The Bragg grating causes the propagating SPP to form Bloch modes. These modes consist of multiple harmonics, all having the same frequency, but a wavevector which is an integer times $2\pi/a$,with a the grating periodicity, higher or lower than the central wavevector.

Furthermore the complex reflectivity of a SPP grating is studied. Reflecting SPPs is the first step in directing SPPs on a nm scale and it is crucial that not only the amplitude reflection is measured, but also the induced phase shift. The more

complex the SPP circuits will become, the more important it is to completely understand the behavior of all individual components. Phase shifts are thus important to take into account. All these results form the start of the investigation of the temporal behavior of SPP devices.

1.5 Outline of this thesis

Chapter 2 will start by explaining the measurement setup used for all measurements described in the thesis. The design requirements are discussed and the implementation of all requirements into the microscope that was realized. Also a theoretical background of how the microscope works, is added. After that the first time- and phase-resolved measurements on propagating SPP wavepackets in a straight SPP guide are presented.

Chapter 3, 4 and 5 discuss what happens if a Bragg grating is created along the straight waveguide. First in chapter 3 we discuss the reflectivity of the induced grating. The complex reflectivity is measured and using that, the phase length is determined. Chapter 4 describes in detail the Bloch behavior of the SPP wavepacket as it propagates along the grating. We show the time evolution of individual Bloch harmonics, all within one Bloch mode, and find that the different harmonics couple differently to the near-field probe. In chapter 5 we show that the group velocity of SPP wavepackets propagating along the SPP grating can be reduced. A reduction of the group velocity by a factor of 2 for a wavepacket with a bandwidth of 4 THz is achieved.

Chapter 2

Novel instrument for surface plasmon polariton tracking in space and time

We describe the realization of a phase-sensitive and ultrafast near-field microscope, optimized for investigation of surface plasmon polariton propagation. The apparatus consists of a home-built near-field microscope that is incorporated in Mach-Zehnder type interferometer which enables heterodyne detection. We show that this microscope is able to measure dynamical properties of both photonic and plasmonic systems with phase sensitivity.

2.1 Introduction

Surface plasmon polaritons (SPPs), which are the solution of Maxwell's equations at the interface between a dielectric and a metal [6, 8], have captured the interest of scientists from a wide range of disciplines. For instance, SPPs are being explored for applications in merging optics and electronics [7] data storage [12], improving conventional microscopy [13] and solar cells [14]. Already they are used in sensors for detecting biologically interesting molecules [38, 39]. Most of these applications require SPP propagation and manipulation on a μm, or even sub-μm scale. SPP properties at these length scales are not easy to model. Therefore, a measurement technique able investigate SPP behavior on a (sub-) μm scale is very valuable. For a complete picture of the SPP behavior, at every position along a SPP device, one would like to know the amplitude and phase of the SPP E-field. In order to investigate the dynamical behavior of SPPs, time-resolved measurements are also required.

The SPPs are bound to a metal-dielectric interface, which makes it complicated to detect them. Imaging their propagation with far-field optics will only work if the SPPs are coupled back to photons first. Four main methods have been reported in literature to detect SPPs. The first method is to detect the leakage radiation [17]. Roughness will scatter SPPs into far-field radiation (photons) that can be detected with a microscope. Drawback of this technique is that one measures the scattered field, rather than the SPP itself, i.e., the scatterer is an integral part of the detected field. The second technique uses fluorescent probes such as dye molecules [18] and Er^{3+} ions [19]. For sufficient low concentrations the probes do not perturb the SPP under investigation, so with this technique one can visualize the bound mode. However, diffraction will limit the resolution of this technique and all phase- and time-information is lost. The third technique to detect SPPs is by photoelectron emission microscopy (PEEM) [40]. This technique obtained time- and phase-sensitivity for SPPs on a grating [20] and a smooth metal film [21] with a subwavelength resolution. An actual movie was presented showing SPP propagation with $<$ 10 fs temporal resolution using PEEM [21]. Unfortunately, PEEM requires (ultra) high vacuum conditions at the sample, which can hinder experiments. Also this technique cannot be used to study photonic systems like photonic crystals. Another technique to study SPP dynamics is by optical pump-probe experiments [41]. Using this technique the authors of ref [41] were able to determine the SPP dephasing and found a momentum lifetime of 48 fs. While pump-probe is a very useful technique for time-resolved experiments, it is generally not a phase resolved technique.

The most common method for studying SPP propagation is by using a near-field microscope [22, 23], or a photon scanning tunnelling microscope (PSTM). In literature results have been shown of near-field measurements on (guided) SPPs [24, 25, 33, 35–37]. These papers show the SPP Bloch behavior on a SPP grating [33], and a full investigation of the near-field distribution of SPPs guided by a metal guide [24]. The influence of the width of the metal guide was examined in terms of mode profile [35] and waveguide cutoff [25, 36]. All these investigations, with the exception of ref [37], measure time-averaged intensity distributions. In this chapter we present a near-field microscope to study SPP behavior with both amplitude and phase information of the SPP E-field. It also allows time-resolved measurements to study SPP dynamics.

This chapter is organized as follows: first the microscope requirements are listed in section 2.2. The realized instrument is described in section 2.3. Section 2.4 and section 2.5 describe the theoretical background of the measurements. In section 2.5.1 and section 2.5.2 the two different measurement schemes possible with the instrument are presented. Experimental results are given in section 2.6.

2.2 Microscope requirements

In order to realize a microscope able to measure phase-sensitive and dynamical properties of propagating SPPs, the following requirements have to be fulfilled:

1. Like all near-field microscopes, the vibrations in the sample holder, probe holder, and optical table can not be larger than 1 nm. They should preferably be even lower. This is because the near-field probe and sample have to be stable with respect to each other in order not to change the amplitude of the signal and to prevent damage to the probe.

2. As will become clear in section 2.4 the complete setup needs to be temperature stabilized and shielded from air flows in order to minimize phase drift in the optical paths.

3. The amplitude and phase of the SPPs should be detected as a function of position.

4. The instrument should allow for time-resolved measurements of SPP propagation.

5. The sample holder should be suitable to investigate plasmonic structures and therefore a prism for the ATR excitation should be mountable (see section 1.2).

The sample holder also needs to accommodate the investigation of photonic structures like photonic crystals, which requires end-fire coupling with either objective lenses or lensed fibers. As a result the sample should be accessible from all sides.

6. A tip scanning microscope, instead of a sample scanning microscope is desired. In a tip scanning microscope the sample will not move with respect to the laboratory frame which greatly facilitates incoupling of incident laser beams.

7. In order to perform time-resolved measurements some sort of pump-probe configuration will be needed. We will show in section 2.5 that for our measurements a delay line must be scanned with nm size steps with a good reproducibility. A delay line with inferometric precision is therefore needed.

2.3 Experimental realization

The near-field probe forms a crucial part of a near-field microscope. Our probes are fabricated as follows. An optical fiber is pulled at both sides while a laser heats the fiber in the middle (Sutter instrument company, Micropipette puller). As the fiber melts, it is pulled apart until it breaks, which results in two sharp tips at both sides. Under the proper heating and pulling conditions a tip with a radius of only a few tens of nm is obtained, combined with a sharp taper (see figure 2.1(a)). To shield the probe from unwanted stray light, it is coated with a metal coating. With focused ion beam (FIB) milling, the end of the probe is polished, resulting in a flat-end faced with a roughness smaller than 10 nm and a well defined circular aperture. An important advantage of FIB treated probes is the reproducibility of the near-field optical measurements [42]. All the measurements presented in this thesis have been performed with a fiber probe that is coated with 200 nm of Al and 5 nm Cr as an adhesion layer. After FIB treatment the apertures have a 100 nm radius, see figure 2.1(b).

As the tip of the probe is brought into the evanescent tail of a (propagating) E-field, e.g., of a SPP, a minute fraction of the evanescent tail is able to couple to the probe. Subsequently, this light is brought to a detector. The detector measures a signal proportional to the intensity of the E-field picked up by the probe which is, in the cases relevant to this thesis, therefore proportional to the field inside the structure.

Because of the exponential decay of the evanescent field, the probe has to be within a few nm of the surface. Also we desire to measure the optical signal and the

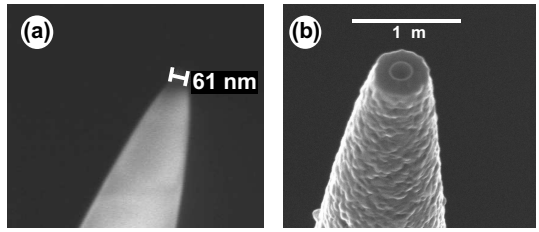

Figure 2.1: *(a): SEM micrograph of a typical near-field probe after pulling. The tip of the probe has a radius of 30 nm. (b): SEM micrograph of a typical coated near-field probe used for the experiments described in this thesis. A probe like the one shown in (a) is coated with a 5 nm Cr adhesion layer and 200 nm Al. With a FIB a 200 nm aperture is fabricated.*

sample topography simultaneously, in order to be able to correlate the two. Two main techniques are possible: the first one is using atomic force microscopy (AFM) in either contact mode, or tapping mode [28], and the second method is shear-force feedback [43]. We chose to work with shear-force feedback because with this technique there will be minimal contact between sample and probe and we avoid potential damage of the sample due to the probe. For shear-force feedback, a fiber which ends in a near-field probe, is glued along the side of one of the prongs of a quartz tuning fork. The bare tuning fork has a resonance of 2^{15} = 32768 Hz. Once a fiber is glued to the fork, the resonance of the fork is shifted a few Hz, and the quality factor (Q) is reduced by several orders of magnitude to a typical value in the range of 200 to 700 [44]. The tuning fork can either be dithered by an external piezo element, or driven electronically, which uses the piezo response of the quartz itself. We chose the first option because this configuration has the best signal to noise ratio [45]. By incorporating an oscillating tuning fork in one branch of an interferometer, we measured that for typical measurement conditions in our system, bending amplitudes are of the order of 1 nm. Because of this small movement and the detector integration time being two orders of magnitude longer than the dither frequency, we can ignore the prong movement on the optical signals for the remainder of the chapter.

The externally driven prong movement in turn causes a measurable piezoelectric potential inside the quartz tuning fork, that is proportional to the tuning fork oscillation amplitude. Typically 10 nm above the surface, the probe-surface interaction becomes measurable. This interaction causes a shift in the resonance frequency and typically also extra damping of the tuning fork. Because the tuning fork is dithered with a constant frequency, the shift in resonance leads to a measurable change in the amplitude and phase of the piezoelectric potential produced by

the quartz tuning fork. The change in phase with respect to the driving phase is measured and used to perform the height feedback [46]. When the probe is raster scanned over a sample, the feedback loop keeps the probe within the evanescent tail of the SPP. In this way the time-averaged SPP intensity at different positions on the sample is measured. From the height feedback signal the topography of the sample is simultaneously obtained with the optical signal.

In order to enable time-resolved measurements an optical delay line is added to the setup. To obtain a feedback motion on the position of the delay line a Heidenhain LIP 372 Exposed Linear Encoder is used. This encoder obtains its position information by counting the individual increments of a periodic structure. It can measure a total travel of 70 mm. The actual motion is achieved with a PI M-014.DP1 translation stage and a M-227.25 DC-actuator, with a 25 mm travel combined with a PI P-840.30 piezo actuator, which has a 45 μm travel and enabling 3.5 nm resolution of the compte system. While scanning the optical delay line, the piezo actuator will take 3.5 nm steps until it reaches its maximum range. At maximum range, the DC-actuator travels 45 μm and the piezo shrinks back correspondingly to its minimum extension. This mode of operation results in a caterpillar-like movement. The linear encoder meanwhile monitors the movement and corrects for deviations from the desired movement.

2.3.1 Sample holder and scanner mount

We chose to mount the sample at right angles to the optical table and designed the sample mount accordingly, see figure 2.2. Thus, we obtain full flexibility in the excitation direction since the sample is easily accessible from all angles in the horizontal plane, and we have enough space for the ATR excitation. This way of mounting fixes only one side of the holder with respect to the scanner. It is a less stable solution than in the case of a sample mounted parallel to the optical table and fixed at three or four sides. Although this choice of sample mounting is expected to give rise to vibrational instabilities, we will show in this section that it is possible to obtain the required stability.

The sample holder needs to be as compact and stable as possible. The 561/562 Series *ULTRAlign*^{TM} Precision Multi-Axis Positioning System from Newport is able to meet the desired stability. Sample holder and stage are connected to each other by the use of an Al bridge. The *ULTRAlign*^{TM} positioning system is also used as a base for the sample holder. Instead of manual spindles, motorized actuators are used for the positioning. The probe approach to the sample is automized using similar motors on the positioning system that holds the scanner. In the

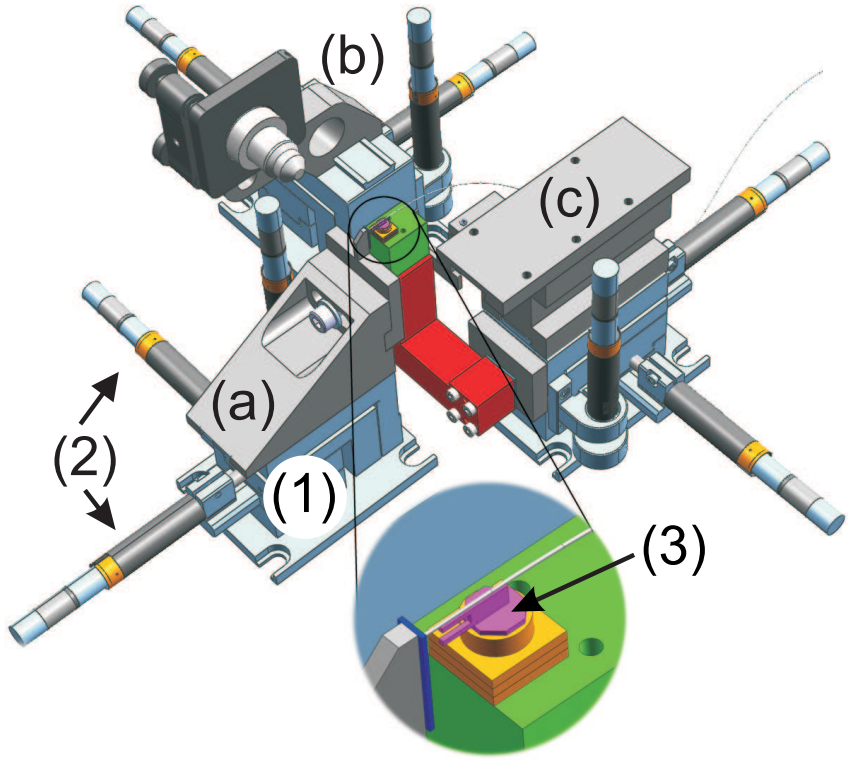

Figure 2.2: *Sketch of the assembled microscope containing the sample holder, part (a), holding a sample depicted in purple, illumination of the sample, part (b) and scanner mounting, part (c). All three parts are mounted on 3-axis ULTRAlign^{TM} positioning systems (1) including motorized stages (2). The x-y probe scanner is shown in red and the z-scanner in green. The pink tuning fork (3) is mounted on a steel base plate, also pink, and fixed in position by a magnet, shown in yellow. The tuning fork is dithered by a piezo shown in yellow.*

automized approach a feedback loop monitors the tuning fork signal to stop the motor-controlled stage movement as soon as a shear force is detected between the near-field probe and the sample surface. The approach is performed with a speed of 2 μm/s and gives a 100% successful approach (excluding human errors). Figure 2.2 shows in light blue (1) the *ULTRAlign*^{TM} positioning systems on which the sample holder (a) is mounted, containing in dark blue the sample, an objective for illumination (b), and the scanner (c). The motorized actuators are indicated by (2).

Mounted on the positioning system is a Piezo Jena series PXY 200 D12 scanner for probe scanning (red part in figure 2.2). It has a 200 μm range in two directions and was customized with an extra thick housing for more vibrational stability. For the z-motion we chose the PZ 20 D12, also from Piezo Jena. The actuator yields a 8 μm range in the direction perpendicular to the sample (green part in figure 2.2). To connect the tuning fork to the scanner, the tuning fork is soldered on a 0.5×0.5 cm steel plate. The plate is in turn fixed in place on the z-piezo with a magnet. In the magnified section of figure 2.2 the tuning fork and steel plate are depicted in pink (3). In the same part of figure the magnet and dither piezo are shown in yellow. The dither piezo is fixed in between the z-piezo and the magnet to excite the tuning fork mechanically. The piezoelectric potential from the quartz tuning fork is amplified by a 100-times pre-amplifier, positioned roughly 2 cm from the tuning fork. The amplified signal is fed into the electronic height-feedback loop. In a real measurement situation it is possible to scan with a scan speeds of the order of 20 μm/s containing 50 nm steps for two weeks non stop without crashing the probe into the sample.

The complete system is shown in figure 2.3. The light path starts with the laser system (1), which generates fs laser pulses. These pulses are split by a beam splitter (2). The necessity for the two branches will be made clear in section 2.4 as the scheme for phase-sensitive measurements is described. The reference branch consists of a delay line (3) and the two AO-modulators (4). It ends at the mixing point (5). In the signal branch SPPs are excited and detected by the near-field probe (6). The probe is scanned in the x-y direction and kept at a constant height above the sample surface in the z-direction so that a height contour of in the sample surface is obtained (7). The E-field in the signal branch and the E-field in the reference branch interfere in mixing point (5). The interference is collected by a detector (8). The detector signal is fed to a lock-in amplifier (9), of which the output is sent to a PC.

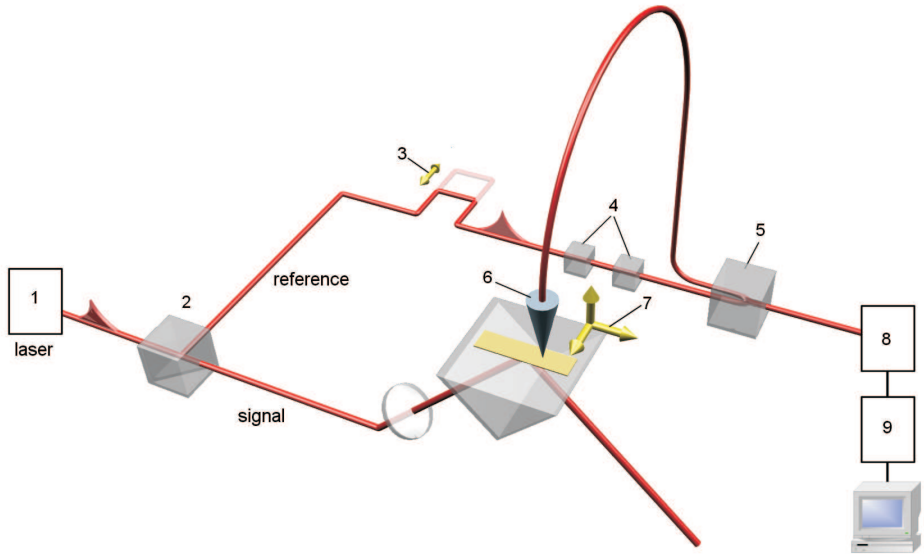

Figure 2.3: *Sketch of the complete setup. In (1) a laser system produces fs pulses, that are split by a beam splitter (2). Inside the reference branch a delay line (3) and two AO-modulators (4) are incorporated. SPPs are excited in the signal branch and picked up by the probe (6), that is actuated in the x,y and z directions (7). The signals from the reference branch and signal branch are mixed (5) and the interference signal is collected by a detector in (8). A lock-in detector (9) processes the detector signal and sends it to a PC.*

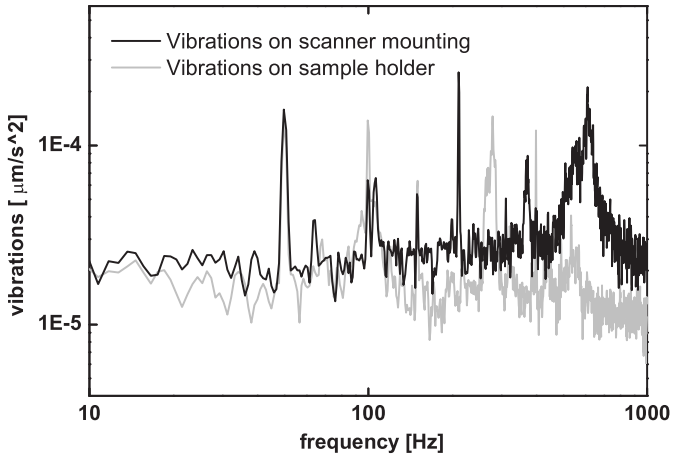

Figure 2.4: *Spectrum of the vibrations on the sample holder ((a) in figure 2.2) and scanner mounting ((c) in figure 2.2), measurement with a calibrated accelerometer during representative experimental conditions. The near-field probe is scanned over the surface and the height control is activate.*

2.3.2 Microscope stability

The complete apparatus is built on an optical table which is passively damped. The complete setup, excluding the electronics and laser system, is enclosed by a box to isolate the optical paths from temperature differences and air drift. Figure 2.4 shows the vibrational spectrum as measured on the sample holder ((a) in figure 2.2) and scanner mounting ((c) in figure 2.2) under standard measurement conditions, i.e., the probe is scanning and kept within a few nm of the surface by the shear-force feedback. Vibrations were measured by placing a calibrated accelerometer (bandwidth: 1 Hz) on both the sample holder and scanner mount. The accelerometers were positioned to measure accelerations perpendicular to the sample surface, which is the most important direction for minimizing vibrations in any scanning probe microscope. Clear resonances are observed in the vibration measurements. However, all of them have accelerations that are orders of magnitude lower than those required for typical commercial scanning electron microscopes. None of the resonances appear in both measurement series, which indicates that the passively damped optical table filters out all vibrations coming from the laboratory environment. Only around 100 Hz a resonance due to cross talk of electrical components is visible in both measurement series.

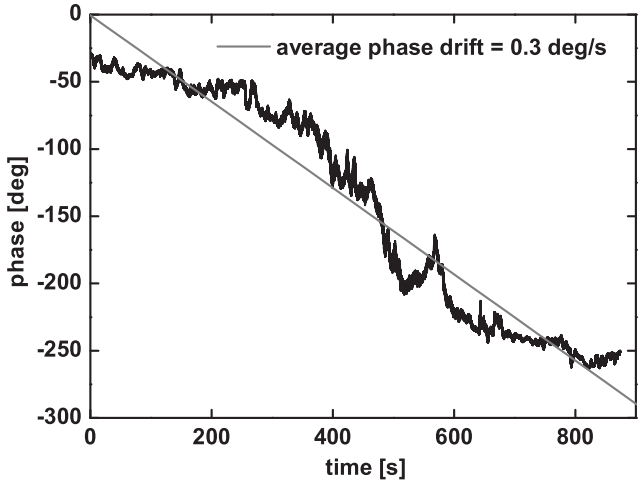

Figure 2.5: *Measurement of the phase drift in the system. For this measurement the near-field probe was kept at a fixed position above a reference waveguide, and the phase information of an E-field inside the guide is monitored in time. From the linear fit we obtain an average phase drift of 0.3 degree per second.*

To quantify the phase drift in the microscope we performed a measurement in which we monitor the phase in a reference waveguide, which is described on section 2.6.1. The phase of the E-field at the position of the probe is monitored over time in a way that will be described in detail in section 2.4. Figure 2.5 shows the result of the phase drift measurement which shows an average phase drift of only 0.3 degree per second. This drift is due to a small temperature drift in the laboratory environment and forms an upper limit. Under typical measurement conditions the phase drift will show a random walk around an average phase.

2.3.3 Electronics

The electronic part of the height-feedback loop is schematically depicted in figure 2.6. During operation the tuning fork (1) is dithered by a piezo driven at the tuning fork resonance by a function generator. The tuning fork typically produces a piezoelectric potential in the order of 1 mV. This is amplified by an amplifier and send to a bandpass module (bandwidth in the order of 1 KHz), which filters around the tuning fork resonance frequency. The phase module determines the

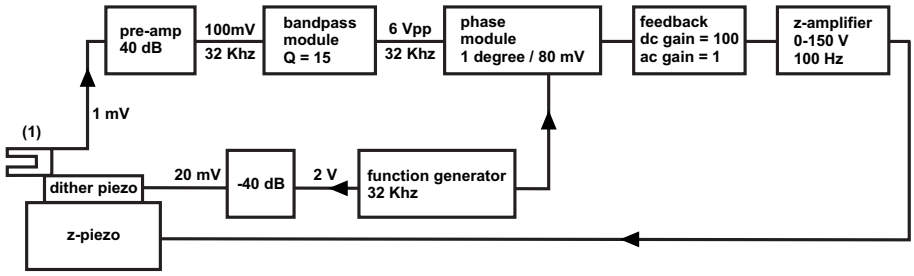

Figure 2.6: *Diagram of the feedback loop used for the shear-force height feedback. At (1) a tuning fork is dithered by a piezo, driven by a function generator. It produces a piezoelectric potential that is amplified by a pre-amp amplifier and sent to a bandpass filter module. The phase of this signal is extracted in a phase module and compared to a reference phase from the function generator. A feedback module, compares the phase from the phase module to a manual set reference phase and provides a feedback signal that is amplified by a high voltage amplifier and sent to the z-piezo. The piezo actuates the probe perpendicular to the sample surface, thus completing the feedback loop.*

phase difference between the filtered signal from the tuning fork and a reference phase from the function generator. In the feedback module, the measured phase difference is compared to a manually set reference phase. With this reference phase, the amount of interaction between sample and probe is set. The feedback module yields a feedback signal that is amplified by a high voltage amplifier and is finally sent to the z-piezo, to control the probe height and thereby completing the feedback loop.

2.4 A phase-sensitive PSTM

In order to obtain phase-sensitive near-field measurements, wee have incorporated the microscope in a (Mach-Zehnder) interferometer [26–29, 32]. Hereto, the light from a laser source is split into two beams to form the branches of the interferometer. One beam is directed to the sample to excite SPPs. A fraction of the E-field is picked up by the near-field probe and brought to the mixing point of the interferometer. This branch (including beam splitter to sample path, propagation in sample and pick-up fiber) is called the signal branch. The other beam is called reference branch and contains an optical delay line and two acoustic-optic modulators to shift the optical frequency.

The following description of the phase-sensitive PSTM is valid for any photonic structure. However, from this point on we will consider the case of SPP detection only, for clarity. The fraction of the SPP E-field that is picked up by the near-field

probe in the signal branch, $E_{sig}(x,y)$, can be described in the following way when continuous wave (CW) excitation is used:

$$E_{sig}(x,y) = A_{sig}(x,y)exp\{i[\omega t + \phi_{sig}(x,y)]\}. \tag{2.1}$$

Here $A_{sig}(x,y)$ is the amplitude of the E-field picked up at position (x,y), ω the frequency of the laser used to excite the SPPs and $\phi_{sig}(x,y)$ the phase of the SPP E-field.

The optical frequency of the light inside the reference branch is shifted by 40 kHz by using two acoustic-optical modulators (AO-modulators). One of the AO-modulators is driven at 80.04 MHz, and the other is driven at 80.00 MHz. The $+1^{st}$ diffraction order of the first AO-modulator is incident on the second AO-modulator of which the -1^{st} order is used in the rest of the reference branch. The E-field in the reference branch, E_{ref}, is described as follows:

$$E_{ref} = A_{ref}exp\{i[(\omega + \Delta\omega)t + \phi_{ref}]\}. \tag{2.2}$$

Here, $\Delta\omega$ is the 40 kHz frequency shift, A_{ref} is the amplitude of the E-field in the reference branch, and ϕ_{ref} the phase of the E-field in the reference branch. At the mixing point E_{sig} and E_{ref} will interfere. The interference signal is detected and the detector measures intensity, I_{det}:

$$I_{det}(x,y) \propto |E_{sig}(x,y)+E_{ref}|^2 = A_{sig}(x,y)^2+A_{ref}^2+2A_{sig}(x,y)A_{ref}cos(\Delta\omega t+\phi(x,y)), \tag{2.3}$$

with $\phi(x,y)$ the effective phase difference between signal and reference branch $(\phi_{ref} - \phi_{sig}(x,y))$. The detector signal is fed into a lock-in amplifier (LIA) which discards the DC terms, and effectively multiplies the remaining with $cos(\Delta\omega t)$. Subsequently, it integrates over a set time T, much longer than $1/\Delta\omega$, i.e., $T > 2,5 \cdot 10^{-5}$ s in our case. In the measurements presented in this thesis $T = 1 \cdot 10^{-3}$ s was chosen. After the integration we are left with an intensity measured by the lock-in $I_{LIA,1}$:

$$\begin{aligned} I_{LIA,1}(x,y) &\propto \frac{1}{T}\int_0^T [cos(\Delta\omega t)][(2A_{sig}(x,y)A_{ref}cos(\Delta\omega t + \phi(x,y))]dt \\ &\propto \frac{2A_{sig}(x,y)A_{ref}}{T}\int_0^T \left[\frac{1}{2}cos\phi(x,y) + \frac{1}{2}cos(2\Delta\omega t + \phi(x,y))\right]dt \\ &\propto A_{sig}(x,y)A_{ref}cos(\phi(x,y)). \end{aligned} \tag{2.4}$$

The LIA also produces a signal that is shifted by 90°:

$$I_{LIA,2}(x,y) \propto A_{sig}(x,y)A_{ref}sin(\phi(x,y)). \tag{2.5}$$

These two results, eq. 2.4 and eq. 2.5, are the two outputs of the lock-in amplifier. They can be combined to obtain a signal I_{SPP} at the measurement position:

$$\begin{aligned} I_{SPP}(x,y) &\propto \left\langle [A_{sig}(x,y)A_{ref}cos(\phi(x,y))]^2 + [A_{sig}(x,y)A_{ref}sin(\phi(x,y))]^2 \right\rangle^{\frac{1}{2}} \\ &\propto A_{sig}(x,y)A_{ref}. \end{aligned} \tag{2.6}$$

Since the amplitude in the reference branch is constant, I_{SPP}, is proportional to the *amplitude* of the SPP E-field at position (x, y). The phase of the SPP E-field relative to a (constant) reference phase, ϕ_{ref}, is given by:

$$\phi_{SPP}(x,y) = arctan\frac{2A_{sig}(x,y)A_{ref}sin(\phi(x,y))}{2A_{sig}(x,y)A_{ref}cos(\phi(x,y))}. \tag{2.7}$$

Note that this $\phi_{SPP}(x, y)$ may contain a possible phase drift in one or both optical branches, due to temperature changes and/or other environmentally induced drifts. The influence of this drift is discussed in section 2.3.2.

For the signal analysis described in the remainder of this thesis we combined the information coming from the two LIA outputs to form a "complex amplitude", $A_{SPP,com}$, of the SPP:

$$A_{SPP,com}(x,y) = I_{LIA,1}(x,y) + i \cdot I_{LIA,2}(x,y). \tag{2.8}$$

This complex amplitude is later in this thesis used in for instance Fourier transforms. In the remainder of this thesis, the amplitude of the SPP E-field is given by the absolute value of $A_{SPP,com}$. The real part of $A_{SPP,com}$ yields what we call in this thesis the amplitude times $cos(\phi)$. This is proportional to the amplitude to the SPP E-field times the cosine of its phase.

Heterodyne detection has another advantage besides phase information: it also increases the system's sensitivity. In a conventional experiment one measures:

$$I_s \propto |A_{sig}|^2. \tag{2.9}$$

Since $I_{SPP} \propto A_{sig}(x, y)A_{ref}$, the heterodyne detection results in a signal enhancement of: A_{ref}/A_{sig}. Since the amplitude inside the reference branch can be made orders of magnitude higher than the signal picked up by the probe, this easily gives a factor > 10 signal-to-noise enhancement in real measurement situations. This means that signals in the order of fW are detectable.

By raster scanning the probe above a waveguide guiding SPPs $A_{SPP}(x, y)$ and $\phi_{SPP}(x, y)$ are measured at different positions. The setup described above will in this case measure a time-averaged E-field distribution, containing the phase information.

2.5 An ultrafast PSTM

The investigation of SPP dynamics uses (fs) laser pulses instead of a CW laser. The limited coherence length of the optical pulse will only result in interference between the pulse in the reference branch and the pulse in the signal branch if they have time overlap on the detector. Thus time-resolved measurements become possible [30]. Two measurement schemes for studying SPP dynamics are possible. In one scheme, the reference branch is fixed in length, and the probe is raster scanned over the surface. Subsequently, the reference branch is made longer or shorter and the measurement is repeated. This scheme is described in section 2.5.1. Alternatively, the probe can be fixed in space with respect to the sample, and the reference branch can be made longer or shorter. This measurement is repeated at different positions of the near-field probe, see section 2.5.2.

2.5.1 Measurement scheme 1: fixed time, scanning probe

In order to describe a measurement using fs pulses extra time dependencies have to be introduced in eq. 2.1 and eq. 2.2:

$$E_{sig}(t) = A_{sig}(x,y,t)exp\{i[\omega t + \phi_{sig}(x,y)]\} \tag{2.10}$$

$$E_{ref}(t-\tau) = A_{ref}(t-\tau)exp\{i[(\omega+\Delta\omega)(t-\tau) + \phi_{ref}]\}, \tag{2.11}$$

with τ a time delay between the two branches. The analysis used in section 2.4 yields:

$$I_{LIA,1}(x,y) \propto cos(\phi(x,y)) \int_0^T A_{sig}(x,y,t)A_{ref}(t-\tau)dt \tag{2.12}$$

and

$$I_{LIA,2}(x,y) \propto sin(\phi(x,y)) \int_0^T A_{sig}(x,y,t)A_{ref}(t-\tau)dt. \tag{2.13}$$

The intensity measured by the LIA will be proportional to the interference integral between the amplitudes in the two branches. For a detailed description of fs pulse tracking see ref. [47]. If one now raster scans the probe above a propagating SPP wavepacket, the position of the probe will determine the length of the signal branch. This way a frame that resembles a snapshot of the propagating SPP pulse in space is visualized for a given time.

2.5.2 Measurement scheme 2: fixed probe position, scanning time

Alternatively, we can fix the near-field probe at a position (x, y) with respect to the sample. This means that ϕ_{sig} and ϕ_{ref} will be constant with respect to each other.

Therefore we neglect all phase terms in the following description. Again, E_{ref} will depend on time t with a delay time τ, set by a delay line. This means the E-fields inside the signal and reference branches can be written as:

$$E_{sig}(t) = A_{sig}(t)exp\{i\omega t\} \tag{2.14}$$

and

$$E_{ref}(t-\tau) = A_{ref}(t-\tau)exp\{i(\omega+\Delta\omega)(t-\tau)\}, \tag{2.15}$$

respectively.

In this configuration the intensity at the detector will be:

$$I_{det}(t-\tau) = A_{sig}(t)^2 + A_{ref}(t-\tau)^2 + 2A_{ref}(t-\tau)A_{sig}(t)cos(-\omega\tau + \Delta\omega t - \Delta\omega\tau). \tag{2.16}$$

Which yields for the output of the lock-in amplifier:

$$I_{LIA}(t-\tau) \propto \frac{1}{T}\int_0^T [cos(\Delta\omega t)][2A_{sig}(t)A_{ref}(t-\tau)cos(-\omega\tau + \Delta\omega t - \Delta\omega\tau)]dt \tag{2.17}$$

For the simplest case of a Gaussian pulse and no dispersion during propagation in the signal branch, this equation can be evaluated as:

$$\begin{aligned} I_{LIA}(\tau) &\propto \frac{2}{T}\int_0^T A_{sig}(t)A_{ref}(t-\tau)dt \int_0^T \frac{1}{2}cos(\Delta\omega t - \tau\{\omega+\Delta\omega\})dt \\ &\propto \frac{1}{2\sqrt{\pi}}exp\Big(-\frac{\tau^2}{4}\Big)cos(\tau\{\omega+\Delta\omega\}). \end{aligned} \tag{2.18}$$

$\Delta\omega$ (40 kHz) is orders of magnitude smaller than the optical frequency of the laser ($\omega \approx 200$ THz) and is therefore neglected in the remainder of this analysis for clarity. For this simplification the two LIA outputs will be:

$$I_{LIA,1}(\tau) \propto \frac{1}{2\sqrt{\pi}}exp\left(-\frac{\tau^2}{4}\right)cos(\tau\omega) \tag{2.19}$$

and:

$$I_{LIA,2}(\tau) \propto \frac{1}{2\sqrt{\pi}}exp\left(-\frac{\tau^2}{4}\right)sin(\tau\omega), \tag{2.20}$$

respectively. It is easy to see now that I_{LIA} will be maximum if the two branches are equal in length, i.e., $\tau = 0$.

Eq. 2.19 and 2.20 differ from eq. 2.12 and 2.13 in the sense that in the previous measurement scheme there was a dependency on position (x, y) since the near-field probe was scanned. If the SPP propagates through a dispersive medium, the interference between the signal and reference branch will be influenced by this

dispersion [47]. In this measurement scheme the influence of dispersion smaller than in the previous.

For a real measurement situation there will be dispersion in the SPP guide, and we have to write the integral in eq. 2.17 as a multiplication in the Fourier domain:

$$\begin{aligned} I_{LIA}(\tau) &\propto \frac{1}{T}\int_0^T E_{sig}(t)E^*_{ref}(t-\tau)dt \\ &\propto \mathcal{F}^{-1}[E_{sig}(\omega)E^*_{ref}(\omega)], \end{aligned} \tag{2.21}$$

see also ref. [48]. This result shows an other difference between this measurement scheme and the previous: the Fast Fourier Transform (FFT) of I_{LIA} gives a signal that is proportional to the product of the optical spectrum of the SPP and the (known) spectrum of the pulse in the reference branch.

2.6 Results

To show that the designed near-field microscope meets all the requirements as stated in section 2.2 we performed two measurements. We start with a ridge waveguide that was studied in detail [27] as a reference to prove that the microscope works and is phase sensitive. By studying this waveguide with this setup we show that the microscope is not only capable of measuring SPPs, but also supports end-fire coupling for photonic systems. In section 2.6.2 we turn to a SPP waveguide. For this guide we prove that the microscope is able to measure SPPs phase-sensitive and ultrafast as was required.

2.6.1 Measurements on a photonic model system

The photonic model system consists of a 2 μm wide Si_3N_4 waveguide on top of thermal oxide. The height of the Si_3N_4 layer is 210 nm and a ridge step of 2 nm is created to form the waveguide. A schematic of the waveguide is shown above figure 2.7(a). Figure 2.7 shows the measurement results when CW HeNe-laser light (free space wavelength = 632.8 nm) is coupled into the waveguide. The total scan range of this measurement is 6.3 μm $\times$ 6.3 μm. In the amplitude image (figure 2.7(a)), the time-averaged, normalized amplitude of the E-field inside the guide is shown. White lines indicate the edges of the guide. Most of the E-field is confined inside the guide and two amplitude beating patterns are visible. One has a period of 180 nm and one has a periodicity of 10 μm (obtained from a different measurement with a longer scan range). The fast beating indicates that a standing wave is formed as light reflects back at the end of the guide and interferes with the incoming light. The

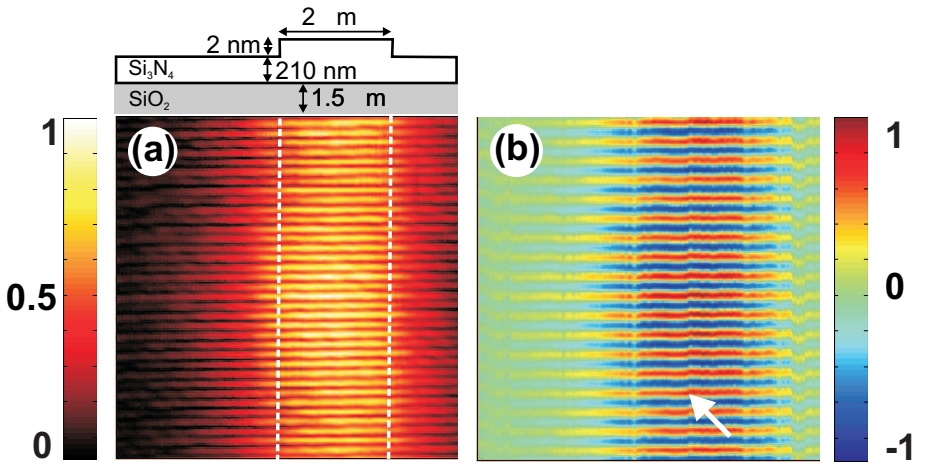

Figure 2.7: *(a): Normalized amplitude measurement of the E-field inside a* 2 μ*m wide, 212 nm high waveguide, incident wavelength CW and 632.8 nm. Scan frame is* 6.3 μ*m squared, scan direction from top to bottom. Above the measurement frame a schematic of the waveguide is shown. White lines indicate the edges of the waveguide in the measurement frame. A periodicity of 180 nm is observed, which indicates a standing wave inside the guide. Also a* 10 μ*m beating is barely visible, which is caused by a spatial mode beating between TE and TM modes. (b): Normalized amplitude times cos(ϕ) of the E-field of the same area as (a), measured simultaneously with (a). Individual phase fringes are resolved, which have a periodicity of 360 nm. The white arrow indicates a phase shift due to phase drift in one of the optical branches.*

slower beating turns out to be spatial mode beating between TE and TM polarized modes. In the normalized phase and amplitude picture, figure 2.7(b), measured simultaneously with figure 2.7(a), individual phase fringes are resolved. Now a clear periodicity of 360 nm is observed, which is in good agreement with the 352 nm wavelength calculated for the TE mode in the guide. The standing wave pattern is no longer visible in figure 2.7(b) because light propagating along the direction of incidence has a higher amplitude than the reflected light.

2.6.2 Measurements on a SPP waveguide

We performed ultrafast and phase-sensitive measurements of SPPs guided by a straight SPP guide. We used the scheme in which we scan the probe and keep the delay line fixed (the scheme described in section 2.5.1). In figure 2.8(a) the topography of the SPP structure under investigation obtained by the shear-force feedback is shown. The guide, a 55 nm thick Au stripe, was prepared lithographically on a glass substrate such that a 6 μm wide Au stripe protrudes from a launch pad.

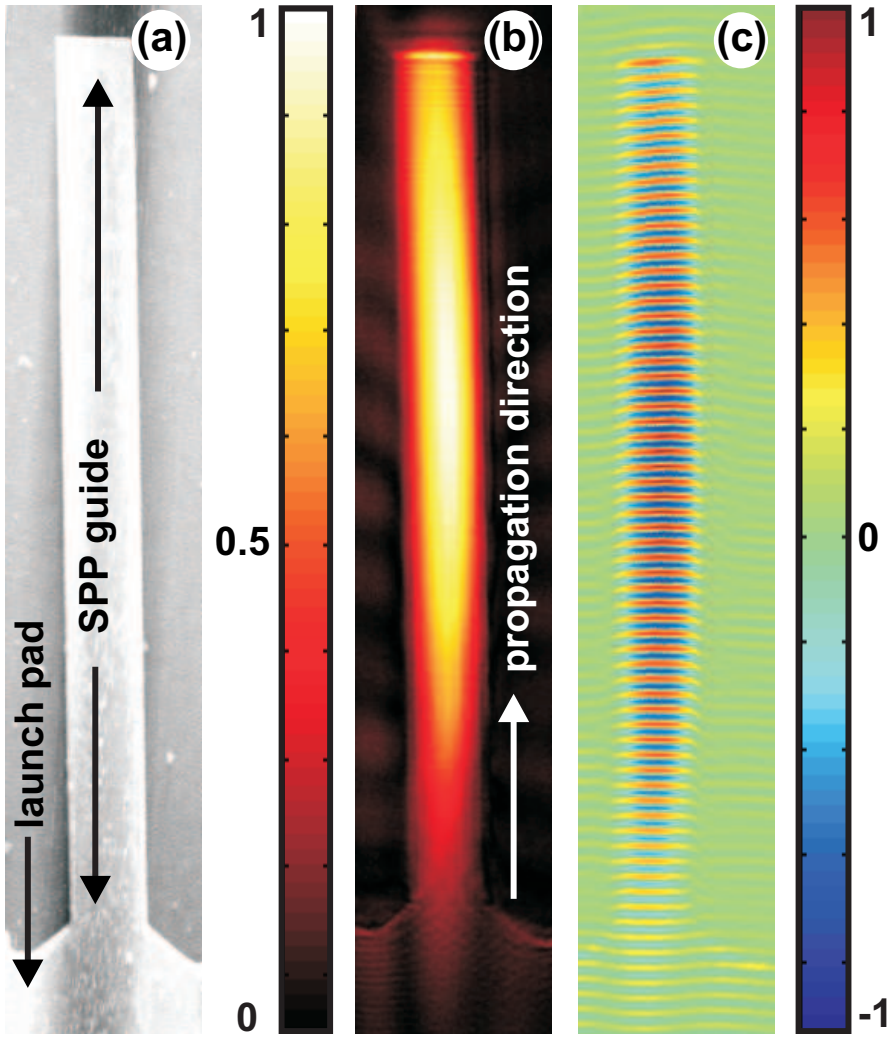

Figure 2.8: *(a): Topography of the SPP waveguide obtained by shear-force feedback. It consists of a 55 nm thick Au guide, 6 µm wide and 80 µm long. (b): Normalized amplitude measurement of the E-field of the SPP wavepacket inside the 6 µm waveguide. (c): Combined phase and amplitude information (∼ Acos(ϕ)) of the same measurement as (b). Scan lines run from top to bottom and the scan frame is 15 µm × 110 µm, wavelength in air used to excite the SPPs: 1500 nm pulses with 20 nm bandwidth.*

Part of this launch pad is visible in the bottom of figure 2.8(a). The total length of the guide is 80 μm. SPPs are excited using the ATR configuration at the gold-air interface of the launch pad using a Ti:Sapphire laser pumped optical parametric oscillator (pulse duration 120 fs, repetition rate 80 MHz, wavelength in air 1500 nm, bandwidth 30 nm). As fs pulses are used to excite the SPPs, fs SPP wavepackets are created.

In figure 2.8(b) we show the normalized amplitude information of the SPP E-field. The probe is scanned from top to bottom of the figure (scan frame 15 μm $\times$ 110 μm) and one frame takes order of 30 minutes measuring time. At the end of the guide SPPs are scattered into photons, the small signal above the guide, and part is reflected back forming a standing wave pattern visible in the top of the guide. The SPP is strongly confined inside the 6 μm Au guide and only a single mode is excited. Theoretical predictions [49] expect that a 6 μm wide guide for the wavelength used should just be able to support two modes. Apparently we only excite one, since no mode beating can be observed. The amplitude FWHM length of the SPP wavepacket is 73 $\pm$ 1 μm, which is in good agreement with the theoretically expected 72 μm, based on a 120 fs pulse.

Figure 2.8(c) shows the normalized amplitude and cosine of the phase of the propagating SPP wavepacket. From this measurement the SPP wavevector is directly obtained by measuring the periodicity of the phase fringes. The SPP wavevector is approximately $4.1 \cdot 10^{-3}$ nm^{-1}, which is roughly 1.02 times the wavevector of the light used to excite the SPPs. This means that the SPP are extremely photon like, but still bound to the Au-air interface.

2.6.3 Time resolved measurements on SPPs

When the SPP wavepacket is probed for different settings of the optical delay line we visualize the wavepacket at different positions in time as it propagates along the guide (figure 2.9(a) up to (e)). Every frame is a new scan of the measurement frame, scan direction again from top to bottom of the figure. The time delay between each frame is determined by the displacement of the delay line of 7.2 μm, corresponding to 48 fs. From this measurement sequence we can study the SPP dynamics in a direct way. Two properties that follow directly from this measurement are SPP group velocity, by following the wavepacket in time, and its amplitude attenuation length, by looking at the decay of the SPP as it propagates, they are $2.5 \cdot 10^8$ m/s and 70 μm, respectively. This amplitude attenuation length corresponds to an intensity attenuation length of 35 μm.

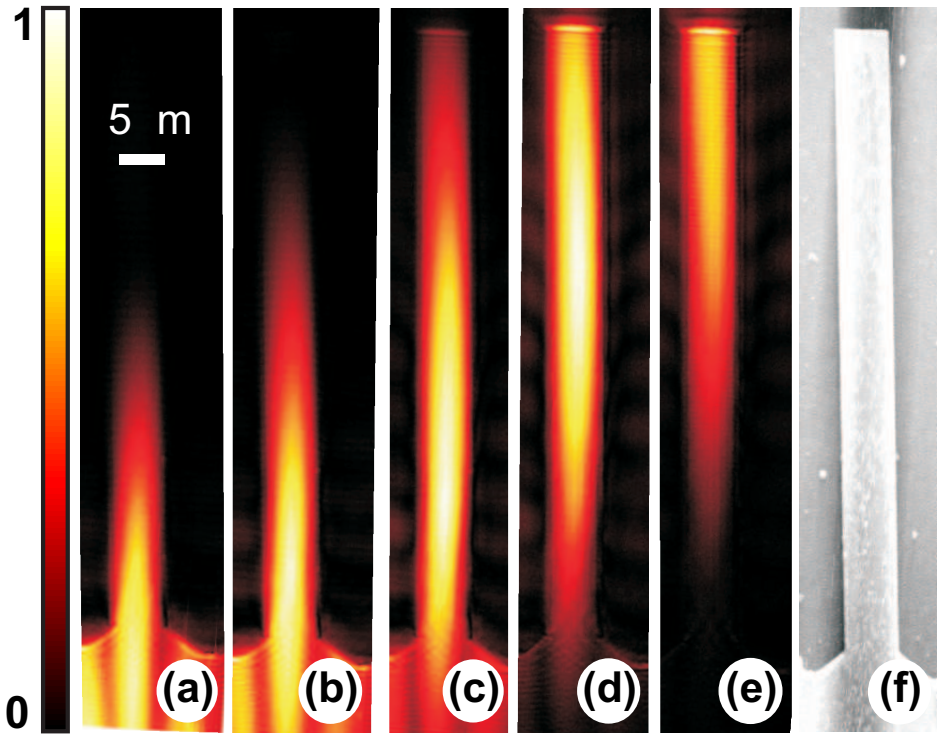

Figure 2.9: *(a) up to (e): Normalized amplitude information of the SPP wavepacket E-field. Succeeding frames are new scans of the probe. In between the frames the delay line is lengthened* 14.4 μm*. Therefore, the time between two frames is 48 fs. Scan frame is* 15 $\mu m \times 110\ \mu m$*, scan lines run from top to bottom. (f): Topography of the SPP waveguide obtained by shear-force feedback.*

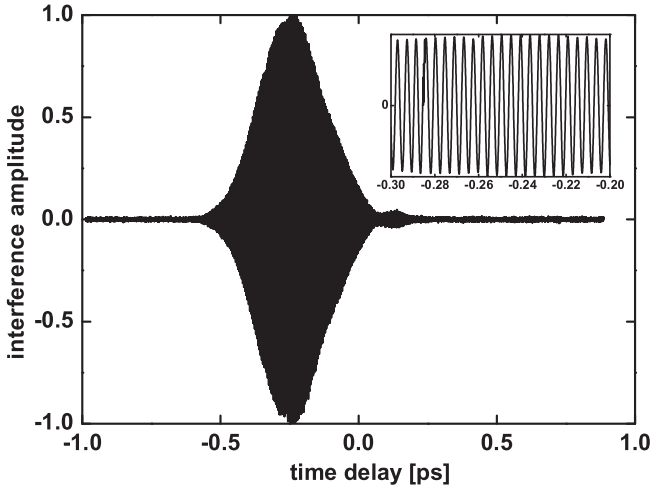

Figure 2.10: *Typical measurement using measurement scheme 2 (see section 2.5.2). The probe is fixed with respect to the sample and the delay line is scanned. In this measurement the probe was fixed at the beginning of the guide used for the measurements described in section 2.6.1. Inset is a zoom in on the center of the interferogram.*

For the measurement described above measurement scheme 1 was used, see section 2.5.1. Figure 2.10 shows the result as measurement scheme 2 (see section 2.5.2) is used at the same structure. The near-field probe is fixed at the entrance of the SPP guide and the delay line is scanned. The result is an cross-correlate between the wavepacket in the reference branch and the SPP wavepacket.

2.7 Conclusions

In the following we will show that all requirements stated in section 2.2 have been met.

1. The stability of the microscope is discussed in section 2.3.2 and turned out to be good enough to measure two weeks non-stop in which the near-field probe maintained within 10 nm of the sample without touching the surface. Also it was possible to observe 2 nm steps in sample topography.

2. In section 2.6.1 we showed that the phase drift in the interferometer is

0.3 degree per second, which is small enough to perform stable measurements.

3. In section 2.3 we showed that it is possible to measure the amplitude and phase of (guided) SPPs.

4. Time-resolved measurements on (guided) SPPs have been obtained and shown in section 2.6.3.

5. In section 2.6.1 we showed that the microscope is also compatible with photonic waveguides.

6. The realized microscope is tip scanning and has a scan range of 200×200 μm as desired.

7. In section 2.3.1 a delay line with interfometric precision is described as was desired and in figure 2.10 it was shown that the delay line can be scanned with the desired position.

Also the basics of near-field microscopy are discussed in this chapter, and the necessary adaptations for time- and phase-resolved measurements are presented. This instrument enables ultrafast investigations of SPP dynamics in metallic nanostructures, of photonic crystal structures and of components for integrated optical circuits.

Chapter 3

Measurements of the complex reflectivity of surface plasmon polaritons on a Bragg grating

The complex reflectivity of surface plasmon polaritons (SPPs) on a SPP Bragg grating is experimentally determined by using phase-sensitive and ultrafast photon scanning tunneling microscopy. It is shown that near the grating stopgap both the amplitude and the phase of the reflection coefficient change significantly. Furthermore, it is possible to determine the so-called phase length. All measurements are in good agreement with a theoretical model based on Rouard's method.

Over the last couple of years there has been an increasing interest in surface plasmon polariton (SPP) optics. SPPs are bound electromagnetic surface waves at the interface between a metal and a dielectric [8], and are of interest because they allow for subwavelength optics [6], integration with electronics [7] and sensitive sensing of biologically interesting molecules [39]. Large progress in propagation length [11] and the realization of passive [34] and active SPP optical elements [50] support the expectations for new plasmonic applications. An important component for SPP manipulation at a micrometer scale is the SPP Bragg grating [51] that can also be used as a SPP mirror [52]. These mirrors are typically characterized by looking at their reflectivity spectrum $R(k) = |r(k)|^2$ [52]. However, it was shown for photonic Bragg structures that the complex reflectivity $r(k)$ provides important additional insight in the properties of the grating like its group delay and dispersion [53, 54]. In this chapter we show measurements of the complex reflectivity of a SPP Bragg grating. The measured reflectivity is found to be in good agreement with a coupled-wave model.

A common technique to detect SPPs is to use a photon scanning tunneling microscope (PSTM) [22]. We used the PSTM described in chapter 2, and the measurement scheme described in section 2.5.1. We have used this technique to measure the phase and amplitude information of a SPP wavepacket propagating along a straight SPP guide and impinging on a SPP Bragg grating. Measurements were performed using femtosecond (fs) wavepackets to determine whether the reflection properties vary on ultrafast timescales. For certain frequencies the grating acts as a mirror and reflects part of the wavepacket. Fourier analysis is used to separate the incoming and reflected SPPs in order to determine the complex reflectivity. Finally the phase shift due to the reflection tells us the position of the grating stopgap and the effective point of reflection inside the SPP grating: the phase length.

3.1 Experimental results

Figure 3.1(a) shows an optical microscopy image of the sample under investigation. It consists of a 55 nm thick Au film in which the structure is fabricated with e-beam lithography and lift off. On the left of the figure a launch pad is visible on which the SPPs are excited on the air-Au interface using a Kretschmann-Raether configuration [9]. The excited SPPs are guided by a 3 μm wide entrance guide to a 55 μm long Bragg grating. The Bragg grating consists of an arrangement of 1 μm indentations with a period of 750 nm leaving an uncorrugated 1 μm Au strip in

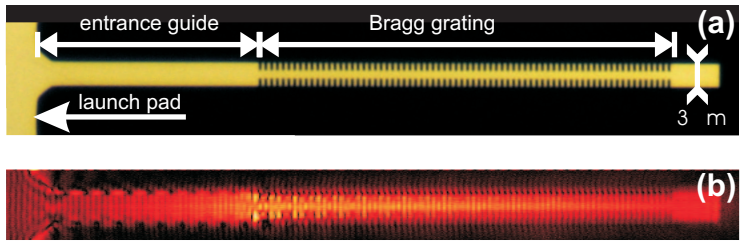

Figure 3.1: *(a): Optical microscope image of the grating under investigation. SPPs are excited at the launch pad and propagate along the entrance guide to the grating. At the interface between grating and entrance guide, part of the SPP wavepacket will be reflected. (b): Amplitude information of the measured time-resolved E-field distribution of a SPP wavepacket. Wavelength in air used to excite the SPPs: 1500 nm.*

the center. Behind the Bragg grating, a small section of unperturbed straight 3 μm wide waveguide is continued. For the excitation of the SPPs we use a Ti:Sapphire laser pumped optical parametric oscillator (pulse duration 120 fs, repetition rate 80 MHz, wavelength tunable between 1400 nm and 1600 nm, bandwidth 30 nm).

The fs SPP wavepackets are measured using a phase-sensitive and ultrafast PSTM. Figure 3.1(b) shows the amplitude information of one measurement frame. For this measurement a fs SPP wavepacket was excited at the launch pad by the fs laser, with a central wavelength (in air) of 1500 nm. At the time were the "snapshot" was taken, the SPP wavepacket has entered the grating via the entrance guide and is concentrated in the center guide in the grating. Along the grating, Bloch waves form, resulting in a periodic amplitude modulation of the SPP E-field as it conforms to the imposed grating periodicity. A detailed study of these Bloch waves is given in chapter 4. An amplitude modulation is also visible in the entrance guide. Because of the stopgap of the grating and also because of an impedance mismatch between the two parts of the structure, part of the SPP wavepacket is reflected back into the entrance guide, resulting in a standing SPP wave.

3.2 Determining the complex reflectivity

To determine the complex reflectivity of the grating we need to know the phase and amplitude of the SPP E-field at the start of the grating of both the incoming, and reflected wavepacket. The raw measurement data contains a superposition of the incident and the reflected SPPs, and need to be separated. To this end the SPP signal along a line trace through the middle of figure 3.1(b) is fast Fourier transformed. The Fourier transform exhibits a Gaussian-like peak with a positive

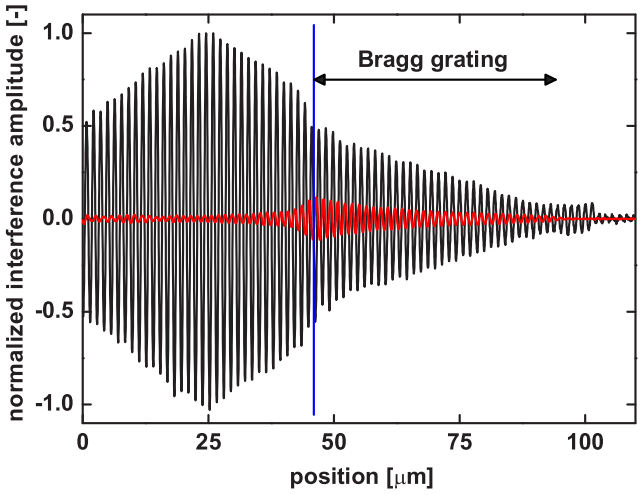

Figure 3.2: *Normalized experimental signal containing both phase and amplitude information of the SPP wavepacket E-field along a line trace through the middle of figure 3.1(b). The measured field with a positive phase velocity propagating in the +x direction (from left to right in figure 3.1(a)) and depicted in black, and the signal with a negative phase velocity, propagating in the -x direction and shown in red are separated by Fourier analysis. The vertical line indicates the end of the entrance guide and start of the grating.*

k-value and a Gaussian-like peak with a negative k-value, corresponding to SPPs traversing the grating in the $+x$ direction (from left to right in figure 3.1(a)), and $-x$ direction, respectively. By selecting only the $+k$ or $-k$ peak in Fourier space and transforming this selection back to real space, we obtain only the SPPs propagating in the $+x$ or $-x$ direction [55, 56]. More details on this Fourier filter technique will be given in section 4.4.1. Normalized phase and amplitude information of the SPP E-field propagating in both directions are shown in figure 3.2 and depicted in different colors. In black the incident SPP wavepacket is shown and the reflected wavepacket, normalized with respect to the incoming amplitude, is shown in red. The vertical line in the figure indicates the boundary between the entrance guide and grating.

Along the grating we also seem to find reflected SPPs, that is with a negative k-value, with an amplitude in the same order of magnitude as in the entrance guide. The SPPs along the grating with a negative k-value are a consequence of the

formation of a Bloch mode [57]. This mode consists of one Bloch harmonic in every Brillouin zone, all separated by $2\pi/a$, where a is the grating period. Because the SPPs are extremely photon like (their wavevector is 1.02 times the wavevector of photons in air at the same frequency), and the small interaction strength between the grating and the SPPs, the Bloch harmonic in the -1 Brillouin zone will have an absolute wavevector close to the incoming SPP, but negative. Therefore, it has almost the same wavevector as the reflected SPPs and the two are virtually indistinguishable in the Fourier analysis. Since we do not consider reflected SPPs inside the grating, we do not have to be concerned about separating the two modes.

We determine the complex reflectivity by considering the amplitude and phase of the SPP E-field at the boundary between unperturbed waveguide and grating. At this transition, the E-field of both the incoming SPP wavepacket, $E_{inc} = A_{inc}exp(i\phi_{inc})$, and the reflected SPP wavepacket $E_{refl} = A_{refl}exp(i\phi_{refl})$ are determined from line traces as shown in figure 3.2, for every excitation wavelength, that is for every incident wavevector k. The complex reflectivity $r(k)$ is given by:

$$r(k) = \frac{A_{refl}(k)}{A_{inc}(k)} exp(i\{\phi_{refl}(k) - \phi_{inc}(k)\}). \tag{3.1}$$

For every excitation wavelength, measurement frames at different times are taken by tuning an optical delay line. It turns out that $r(k)$ does not change in time for the timescales considered in the experiment: order of 100 fs. Therefore, $r(k)$ is determined by averaging over multiple time frames to obtain better statistics.

The amplitude of the complex reflectivity $|r(k)|$ is presented in figure 3.3(a). Measurements were performed for eight different excitation wavelength (bandwidth ranging between 20 nm and 30 nm). For every measurement the amplitude reflection and phase shift are determined. Error bars represent the standard deviation of the values found in all the time frames. The observed increase in $|r(k)|$ around 1475 nm originates from the presence of a stopgap. The position of the stopgap is consistent with measurements shown in chapter 4 and chapter 5.

3.3 Comparison with Rouard's method

The complex reflectivity of a grating can be modelled using Rouard's method as described in ref. [58]. The method is a simplification of the coupled-wave equations and only has two free parameters: the position of the stopgap and the interaction strength between SPP and grating. In figure 3.3(a) a fit through the measurement data is shown in blue, using the absolute value of the complex reflectivity calculated

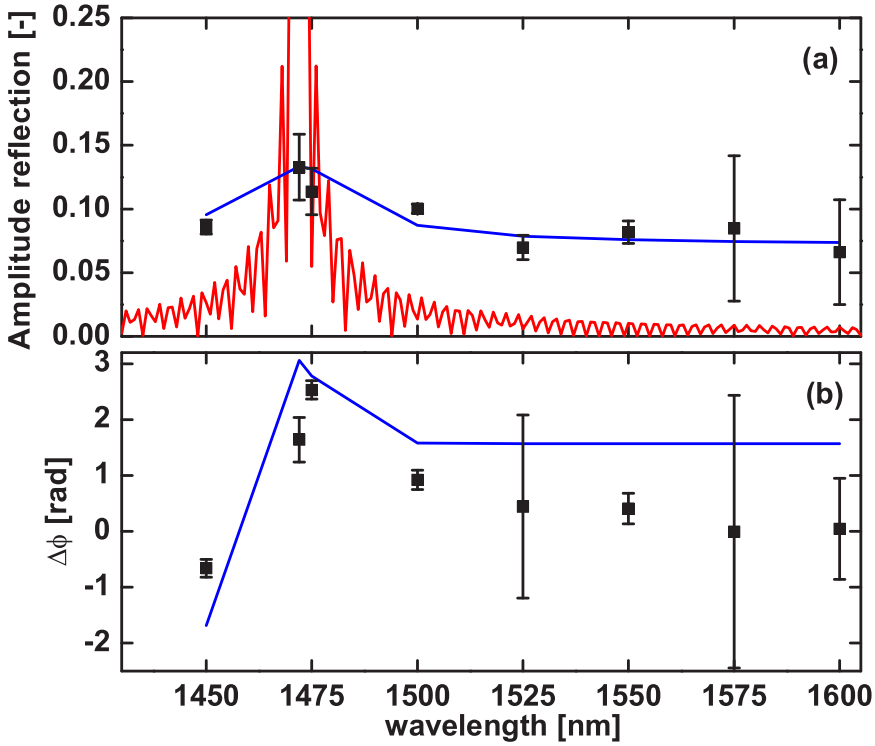

Figure 3.3: *(a): Amplitude reflection of the Bragg grating under investigation. In blue a fit using Rouard's method is shown, when taking into account the bandwidth of the SPP wavepacket and an offset due to impedance mismatch. Excluding the bandwidth and offset leads to the red curve. Error bars are the standard deviation obtained in the multiple time frames. (b): Measurements of the phase shift due to the reflection. In blue the phase reflection of the fitted amplitude reflection shown in (a) is shown.*

with Rouard's method and taking into account the (known) bandwidth of the SPP wavepacket.

Because Rouard's method assumes a transition between the entrance guide and the grating without intrinsic impedance mismatch, far away from the stopgap $|r(k)|$ will tend to zero. However, in the real measurement situation, impedance mismatch does occur. Therefore, a third fit parameter is introduced: a wavelength-independent offset to describe the impedance mismatch. With an offset of 0.07 we obtain a good agreement with the measurement data. This value of $|r(k)| = 0.07$ far away from the stopgap is similar to that of reflections from an abrupt end of an Au SPP guide as we show in section 3.4. In the same figure, in red the calculated amplitude reflectivity is shown for the same grating, without taking into account the bandwidth of the wavepacket and the offset.

With the values of the stopgap position and coupling strength obtained from the absolute complex reflectivity we can predict the phase shift $\Delta\phi = \phi_{refl} - \phi_{inc}$. In figure 3.3(b) the measured phase shift, due to the reflection is shown. Error bars are again the standard deviation that follows from considering multiple time frames. At 1475 nm a jump in the phase is observed, caused by the presence of the stopgap. The phase part of the fitted complex reflectivity in figure 3.3(a), neglecting the offset of $|r(k)| = 0.07$, is also shown in figure 3.3(b). Apart from an offset of 0.5 rad, the calculated $\Delta\phi$ follows the trend of the measurements. This offset in the phase shift has probably the same origin as the (excluded) offset in the absolute value of the complex reflectivity. It is however not possible to predict the measured phase offset using the measured quantities. Note here that we used no additional fitting parameters to calculate $\Delta\phi$.

3.3.1 Grating phase length

Bruyant *et al*. [54] show that the phase shift $\Delta\phi$ caused by reflection of a grating at position x away from the grating, as a function of k can be written as:

$$\Delta\phi(x,k) = 2k(x_{eff} - x), \tag{3.2}$$

where x_{eff} is the effective distance into the grating at which the wave is reflected. The phase length l_{eff} is defined as: $l_{eff} = x_{eff} - x$ and corresponds to the physical distance between the point at which the measurement is performed, x, and an effective interface of reflection, x_{eff}. It is assumed that Fresnel reflections induce a zero phase shift. In a medium without dispersion, phase and group velocity will be equal, and as a result the phase length will be constant. However, close to a band edge, large dispersion effects are expected and the phase and group velocity

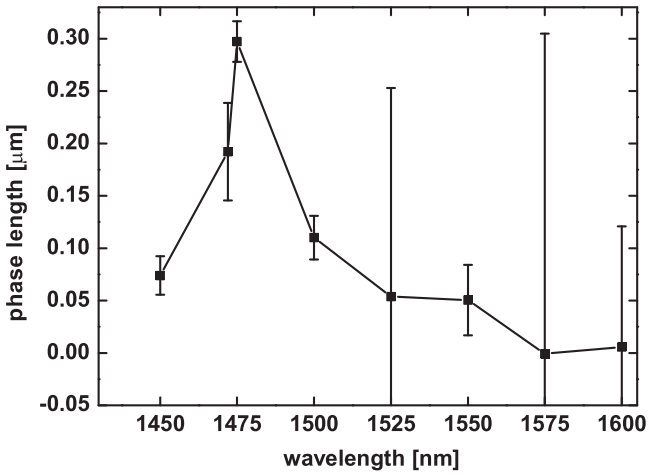

Figure 3.4: *Phase length l_{eff} as a function of excitation wavelength.*

will not be equal anymore. As a result, the phase length will increase.

Our measurement position is at the transition between the unperturbed guide and the grating $x = 0$, which results in $l_{eff} = x_{eff}$, which means:

$$\Delta\phi(k) = 2k(l_{eff}). \tag{3.3}$$

We can determine the k of the SPPs inside the grating for different frequencies by Fourier analysis of the measurement frames containing the amplitude and phase information [27, 56]. Combining these measured values of the wavevector with the measured phase shift in eq. 3.3 directly yields the phase length. Figure 3.4 depicts the determined phase lengths for different excitation wavelength. Because both $\Delta\phi(k)$ and k are measured for the complete bandwidth of wavepackets, the found phase length is also applicable for the full bandwidth of the SPP wavepacket. We observe that close to the stopgap, the phase length reaches values of 0.3 μm.

3.4 Reflection at an abrupt waveguide end

As a comparison, we also looked at the reflection at an abrupt end of a SPP waveguide. For this, we used a straight, 6 μm wide and 55 nm thick Au guide, prepared in the same way as the grating structures. Measurements were only performed

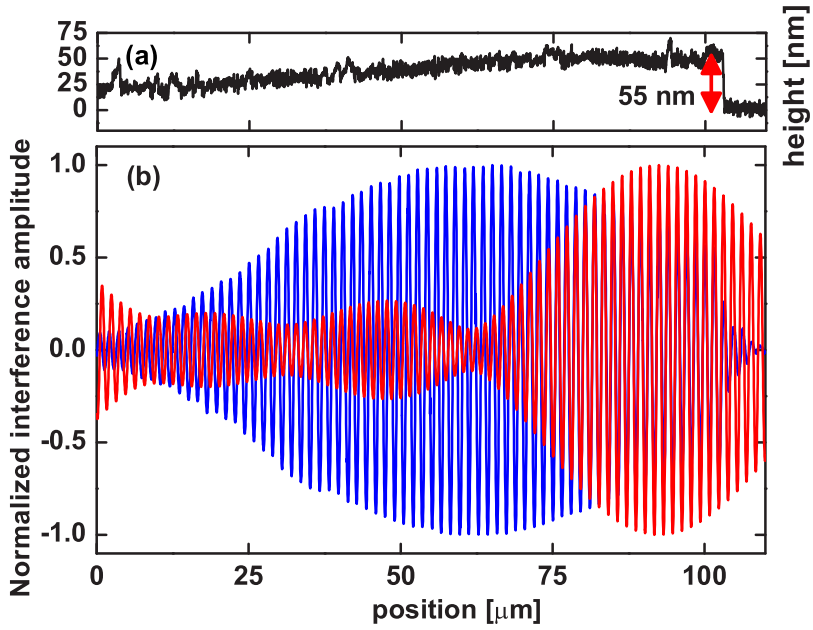

Figure 3.5: *(a): Topography of the studied waveguide measured by shear-force feedback. The step in the topography around* 100 μm *indicates the end of the 55 nm thick waveguide. (b): Normalized complex amplitude of an incoming SPP wavepacket in blue, and a reflected wavepacket, in red. Lines are taken through the center of a* 6 μm *Au guide.*

using SPP wavepackets with a center wavelength of 1500 nm. Multiple time frames are taken to improve statistics. Figure 3.5(b) shows the amplitude of the E-field of the incoming SPP wavepacket and the reflected wavepacket taken along a line in the center of the guide. Both the incoming and reflected amplitudes are normalized to their own maximum value. Separation of the incident and reflected wavepackets is achieved by Fourier analysis as explained in section 3.2 and the definitions of positive and negative phase velocity are the same as in figure 3.2. The two oscillations visible in the reflected SPPs between 0 and 60 μm are a consequence of the FFT filtering. Figure 3.5(a) depicts the topography as measured by the shear-force feedback [44] along the line used to obtain the E-field information. It shows a slightly tilted straight waveguide with an abrupt end at 105 μm at which the SPP wavepacket is reflected.

The measured absolute value of the complex reflectivity is 0.017 $\pm$ 0.002 and the

phase shift is found to be -3.01 ± 0.33 rad. Because Rouard's method is not useful in modelling the straight waveguide, we used Fresnel reflection to compare with the measurements. Using the complex dielectric constant of the Au guide, measured with ellipsometry, in the Fresnel equation for E-fields parallel to the interface of reflection, and normal incidence, gives an absolute value of the complex reflectivity of 0.0029. The phase shift due to the reflection is calculated to be -3.031 rad. The calculated and measured phase shift agree very well. However, there is factor five mismatch between the measured and calculated amplitude reflection, which we can not explain at the moment. Note that the amplitude reflection of the Bragg grating is a factor four higher than the amplitude reflection of an abrupt end of the waveguide.

In conclusion, we have measured the complex reflectivity of a SPP Bragg grating. With a phase-sensitive and ultrafast PSTM it was possible to show that both the amplitude reflection and the phase shift in reflection change significantly around the grating stopgap. Also the grating phase length increased at the grating stopgap. The found complex reflectivity is in good agreement with a model based on Rouard's method.

Chapter 4

Near-field distribution and near-field coupling of surface plasmon polariton Bloch harmonics

The Bloch nature of surface plasmon polaritons in a one dimensional plasmonic crystal is directly observed using ultrafast and phase-sensitive near-field microscopy. Individual Bloch harmonics within one Bloch mode are separated and visualized. Different harmonics within the same Bloch mode turn out to have a different lateral amplitude distribution. The coupling between the different Bloch harmonics and a near-field probe is studied by comparing the found energy distribution over the different harmonics to the theoretically expected distribution. It is found that higher order harmonics couple more efficiently to the probe than lower order harmonics.

4.1 Introduction

When a wave propagates through an infinite periodic medium, Bloch's theorem has to be obeyed [57]. As a result, Bloch modes will form, each consisting of multiple spatial Fourier components. The Bloch harmonics have a wavevector that is an integer times $2\pi/a$ (with a the grating period) separated and will appear in all Brillouin zones in the dispersion diagram. The different harmonics have an identical group velocity and are bound together by the periodic potential, forming a discrete group of coherent waves, without any redistribution of energy [59]. An individual Bloch harmonic will in general not satisfy Maxwell's equations for the periodic medium and therefore can not exist on their own.

The physics of the interaction between waves and a periodic potential is equal for electrons [60], phonons [56, 61], photons in photonic crystals [55], or optically induced latices [62] and surface plasmon polaritons (SPPs) [63]. Studying Bloch modes provides insight in the dispersion of the phononic, photonic or plasmonic crystal, and reveals group and phase velocities. Also the ratio between the amplitude of the different harmonics provides an elegant way of determining extremely small variations in the refractive index due to the periodic potential of the crystal [33]. A way to investigate Bloch modes in optical systems is by looking at scattered photons in the far-field [64]. However, this method relies on imperfections in the structure to scatter the photons out of their bound mode. In addition, a microscope objective of which the spatial resolution is limited by diffraction is used to collect the scattered photons. It has been shown that a photon scanning tunneling microscope (PSTM) is able to resolve the different optical Bloch modes, and also their harmonics, inside a photonic crystal waveguide [33, 55, 65, 66]. The individual Bloch harmonics turned out to have different lateral mode profiles [55].

In this chapter we show the visualization of the different Bloch harmonics present within one plasmonic Bloch mode. An ultrafast PSTM makes it possible to study the development of the individual harmonics in space and time. Moreover, by comparing the experimental results to the analytically calculated energy distribution over the different harmonics, we were able to extract the relative coupling efficiency of the different harmonics to the near-field probe. Since higher harmonics have a larger wavevector, the effective wavelength of the harmonic will be smaller than the near-field probe aperture. This causes significant changes in the coupling efficiency between the near-field probe and the Bloch harmonic.

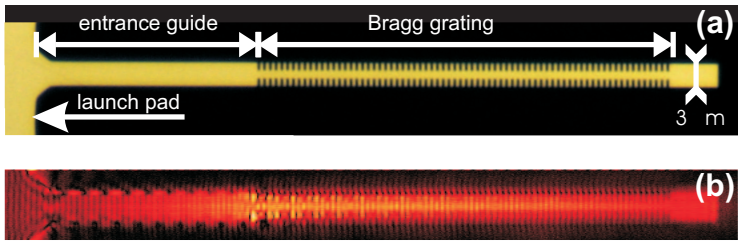

Figure 4.1: *(a): Optical microscope picture of the SPP grating under investigation. SPPs are excited at the launch pad at the left of the figure. They propagate via an entrance guide to a 55 μm long Bragg grating. The Bragg grating consists of periodic indentations of 1 μm (period 750 nm) leaving a 1 μm Au strip at the center. (b): Typical experimentally measured snapshot of the amplitude of the SPP field as obtained with the time-sensitive and phase-resolved PSTM. SPPs were excited with 120 fs pulses with a central wavelength in air of 1500 nm.*

4.2 Experimental aspects

A SPP crystal [51], similar as the one used in chapter 3 was used in this study as a model structure. SPPs are excited on an Au-air interface with light from a Ti:Sapphire laser pumped optical parametric oscillator (pulse duration 120 fs, repetition rate 80 MHz, wavelength tunable between 1400 nm and 1600 nm, bandwidth 30 nm). Figure 4.1(a) shows an optical microscopy picture of the SPP crystal. It consists of a 55 nm thick Au film on BK7-glass and is prepared by e-beam lithography and lift off. At the left of the figure a launch pad is visible on which the SPPs are excited using a Kretschmann-Raether configuration [9]. Via a tapered entrance, SPPs are guided by a 3 μm wide entrance guide of 30 μm long, to a 55 μm long Bragg grating which is created along the straight guide. The Bragg grating consists of an arrangement of 1 μm indentations with a period of 750 nm, thus leaving a 1 μm Au strip remaining at the center. After the Bragg grating, 6 μm of unperturbed straight waveguide is continued. We used the PSTM as described in chapter 2 to study the SPP Bloch behavior.

4.3 Fourier analysis

The general expression for a single infinitely extending Bloch mode at time t and position $\mathbf{r}$ is given by:

$$E(\mathbf{r},t) = \sum_m C_m(\mathbf{k}) exp\left[i\left(\left\{\mathbf{k} + \frac{2\pi m}{a}\right\} \cdot r - \omega t\right)\right]. \tag{4.1}$$

Here m is an integer labeling the harmonic, ω is the angular frequency, $\mathbf{k}$ is the 2D wave vector, a is the grating period and $C_m(\mathbf{k})$ is the complex amplitude of each Bloch harmonic. We will use a two dimensional fast Fourier transform (FFT) to analyze the SPP-field in the two dimensional measurements and to obtain the different wavevectors present. This can be understood in the following way: take the 2D FFT of the SPP-field $E(\mathbf{r}, t)$, to be [56, 61]:

$$F(\mathbf{k}, \omega) = \frac{1}{(2\pi)^2} \int \int_{-\infty}^{+\infty} E(\mathbf{r}, t) exp[i(-\mathbf{k} \cdot \mathbf{r})] d^2\mathbf{r}, \tag{4.2}$$

And take the general Bloch expansion of the SPP E-field, which is:

$$E(\mathbf{r}, t) = Re \sum_n \int \int_{1stBZ} \sum_m C_{n,m}(\mathbf{k}) \times exp\left[i\left(\mathbf{k} + \frac{2\pi m}{a}\mathbf{i}\right) \cdot \mathbf{r} \right] d^2\mathbf{k}. \tag{4.3}$$

Here $\mathbf{i}$ is the x-direction unit vector and n in integer indicating the mode number. Because the E-field is detected by a near-field probe we have to consider a detection efficiency $A_{n,m}(\mathbf{k})$ for each Bloch eigenstate for all different $\mathbf{k}$. Every Bloch harmonic has a different wavevector. This difference can cause a difference in coupling to the probe for different harmonics [67] and must therefore be taken into account. Including $A_{n,m}(\mathbf{k})$ and taking $-\infty < \mathbf{k} < +\infty$, evaluating eq. 4.2 and eq. 4.3 result in:

$$F_{n,m}(\mathbf{k}) = \frac{1}{2} \sum_n A_{n,m}(\mathbf{k}) C_{n,m}(\mathbf{k}) \delta\{\omega - \omega_n(\mathbf{k})\}. \tag{4.4}$$

This result means that the two dimensional spatial FFT of the SPP field, $F_{n,m}$, will be proportional to the amplitude of the Bloch harmonic, $C_{n,m}(\mathbf{k})$, times its detection efficiency $A_{n,m}(\mathbf{k})$. In the experiments that will follow we only excite one Bloch mode, and therefore the mode index n is neglected in the remainder of this chapter.

4.4 Experimental results

For the measurements we raster scan the near-field probe over the Bragg grating while keeping the delay line fixed, which results in a typical snapshot of the propagating SPP as is shown in figure 4.1(b). In the figure we only depict the amplitude information of the SPP-field. The phase information which is obtained simultaneously, is not shown. Already it is visible that the optical field above the grating has a periodic modulation, parallel to the propagation direction (from left to right). The observed periodicity is 750 nm, which is equal to the grating period. We therefore observe that the SPP field conforms to the grating period and forms a Bloch wave. In the entrance guide a standing wave pattern is visible,

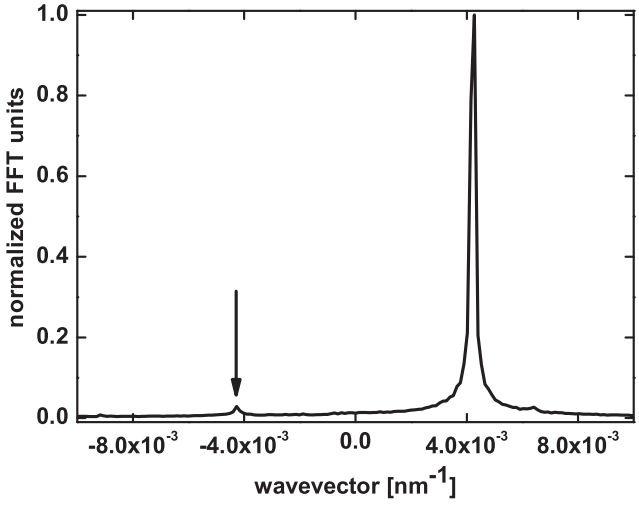

Figure 4.2: *Normalized amplitude of the sum of the 2D spatial FFT of the entrance guide in the direction perpendicular to the grating. Around* $4.2 \cdot 10^{-3}$ *nm*$^{-1}$ *the SPPs propagating from left to right in figure 4.1(b) appear. The SPPs reflected at the interface between the entrance guide and grating have a negative group and phase velocity and appear at* $-4.2 \cdot 10^{-3}$ *nm*$^{-1}$*, indicated by the arrow.*

due to reflections at the transition between the entrance guide and the grating. In the following paragraphs it will become clear how we can discriminate between reflected SPPs and Bloch harmonics.

4.4.1 Separating reflected SPPs and Bloch harmonics

By selecting a part of the real space scan frame, and Fourier transforming only the experimental data in this section, one obtains the spatial frequencies of the selected scan area only. Figure 4.2 shows the result of a 2D FFT of the entrance guide, for a central excitation wavelength of 1500 nm. The 2D amplitude and phase data are summed after the FFT in the direction perpendicular to the propagation direction. The peak around $4.2 \cdot 10^{-3}$ nm^{-1} corresponds to the SPPs propagating in the entrance waveguide towards the grating. The peak around $-4.2 \cdot 10^{-3}$ nm^{-1} (indicated by an arrow) corresponds to the SPPs that have been reflected at the transition of the entrance guide and the grating. These SPPs have a negative phase velocity, since

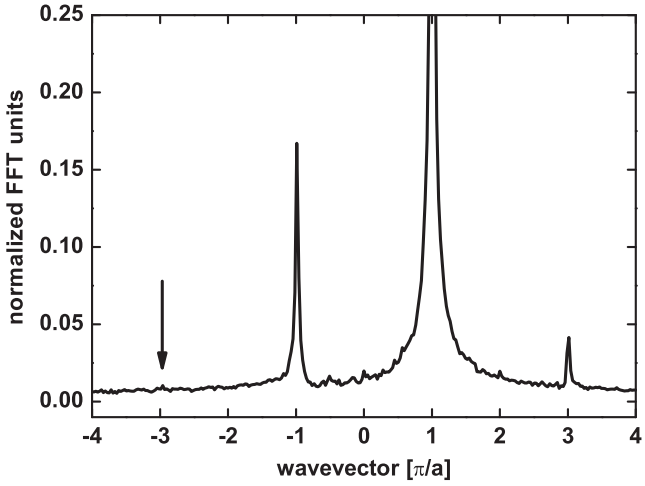

Figure 4.3: *Absolute value of the 2D spatial FFT of the amplitude of the SPP E-field guide in between the grating. Close to π/a the fundamental mode is visible and close to $-3\pi/a$ (indicated by the arrow), $-\pi/a$ and $3\pi/a$ the Bloch harmonics appear.*

their wavevector is negative. The measured magnitude of the wavevector of the SPPs is a factor 1.02 higher than that of photons with a wavelength of 1500 nm in air. This does mean that the SPPs in the waveguide have a strong photon-like character. However, they are still bound since the magnitude of their wavevector is larger than that of photons in air at the same frequency (their dispersion curve lies below the so-called lightline). The sign of the group velocity of the SPPs at $-4.2 \cdot 10^{-3}$ nm^{-1} turns out to be negative if we follow the propagation direction of the mode in time as we will describe in section 4.4.2. Since these SPPs propagate in the opposite direction with respect to the initially excited SPP, we know that they have to be reflected. Interference between the two opposite propagating SPP wavepackets causes the standing wave pattern visible in the entrance guide in figure 4.1(b). The ratio between the peak at $4.2 \cdot 10^{-3}$ nm^{-1} and $-4.2 \cdot 10^{-3}$ nm^{-1} gives the amplitude reflection coefficient, which is $7 \pm 2\%$. We have discussed this reflection in more detail in chapter 3.

Next we select only the fields detected along the guide in between the corrugations. In first instance we do not consider the measured SPP field above the grating to avoid topographical artifacts [68]. The absolute value of the 2D FFT of the SPP

amplitude at this section is shown in figure 4.3, again for an excitation wavelength of 1500 nm in air and summed after the FFT in the direction perpendicular to the propagation direction. Multiple peaks appear, representing individual Bloch harmonics, separated by $2\pi/a$: $-3\pi/a+\epsilon$ (indicated by an arrow), $-\pi/a+\epsilon$, $\pi/a+\epsilon$ and $3\pi/a+\epsilon$, with $\epsilon = 0.015$ nm^{-1} for this frequency. The sign of the group velocity of the different harmonics, $\partial\omega/\partial k$, can be determined by following their propagation as we will describe in section 4.4.2. All harmonics turn out to have a positive group velocity, and are thus part of the same Bloch mode.

The finding that the SPP wavevector is very close to the wavevector of photons in air at the same frequency, combined with the finite length of the grating (55 μm), which results in a finite resolution of the FFT analysis of $1.1 \cdot 10^{-4}$ nm^{-1}, has implications for the analysis of the results. The $m = -1$ Bloch harmonic and reflection of the $m = 0$ harmonic at the end of the grating, will both end up at the same position in the 2D FFT, i.e., at roughly $-\pi/a = -4.2 \cdot 10^{-3}$ nm^{-1}. Easy separation is only possible at frequencies for which $|\mathbf{k}| \neq \pi/a \pm 1.1 \cdot 10^{-4}$ nm^{-1}. At such frequencies our phase-sensitive microscope will yield two distinguishable peaks. Figure 4.4 shows that for an excitation wavelength in air of 1600 nm this is indeed the case. The peak at the left is the $m = 1$ Bloch harmonic and the peak on the right is SPPs reflected at the end of the grating. We are able to discriminate the two by looking at their group velocity.

Since in this study we focus on the behavior of the Bloch harmonic and not on the reflected SPPs, the amplitude of the Fourier peaks around $\mathbf{k} = -\pi/a$ should be corrected for the reflected SPPs to arrive at the detected signal of the $m = -1$ Bloch harmonic. Averaging over multiple measurements, all with different delay line positions, gave a ratio $F_{-1}/r = 5.5$, with r being the amplitude of the reflected SPPs. F_{-1} and r were determined by taking the peak value of the two individual peaks. This procedure turned out to give the same results as fitting two Gaussians to the graphs. If we assume this ratio to be independent of frequency, at all frequencies: $F_{-1} = \mathfrak{I}(\mathbf{k})/(1 + \frac{1}{5.5}) = \mathfrak{I}(\mathbf{k})/1.18$, with $\mathfrak{I}(\mathbf{k})$ the total FFT amplitude found at $-\pi/a$. Once the Bloch harmonic and the reflection are separated, it is possible to determine the amplitude reflection coefficient of the end of the grating. This coefficient is in the same order of magnitude as for entering the grating: $4 \pm 1\%$. If we assume that all Bloch harmonics will experience the same reflection, the amplitude of the reflection of the $m = +1$ harmonic would be one order of magnitude smaller than the amplitude of the Fourier peak at the position of the $m = -2$ harmonic, that will have roughly the same wavevector as the reflection of the $m = +1$ harmonic. Since the reflection of the $m = +1$ harmonic is also not visible in figure 4.4, we can and will neglect the reflections of the Bloch harmonics with $m \neq 0$.

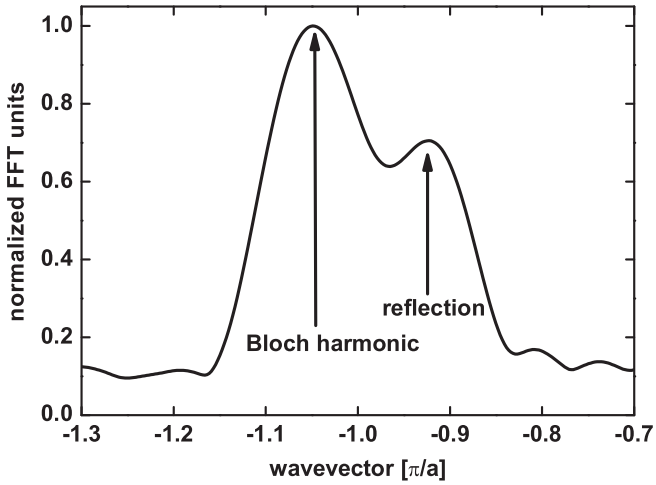

Figure 4.4: *At an excitation wavelength of 1600 nm the $m = -1$ Bloch harmonic and the reflected SPPs are distinguishable. The peak at the left is the Bloch harmonic and the peak on the right is the reflection.*

$F_n(\mathbf{k})$ is determined for different reference times, i.e., for different positions of the SPP wavepacket along the guide. The result is depicted in figure 4.5. The figure contains the relative values of $F_m(\mathbf{k})$, normalized to $F_0(\mathbf{k})$. No clear trend in time is observed for any of the Bloch harmonics. Fluctuations of $F_m(\mathbf{k})$ in time are explained by experimental noise, caused by temperature drifts and mechanical vibrations. The absence of a trend in figure 4.5 means that as the Bloch mode is excited, all energy within the mode is instantaneously distributed over the different harmonics. This observation is in agreement with predictions by Russell [59], who stated that Bloch harmonics propagate as a unity without any redistribution of energy. We can therefore take $F_m(\mathbf{k})$, $C_m(\mathbf{k})$ and $A_m(\mathbf{k})$ to be constant in time in the rest of this investigation. All values of $F_m(\mathbf{k})$, $C_m(\mathbf{k})$ and $A_m(\mathbf{k})$ in the remainder of this chapter will be the average of values obtained at different time steps to enhance statistics.

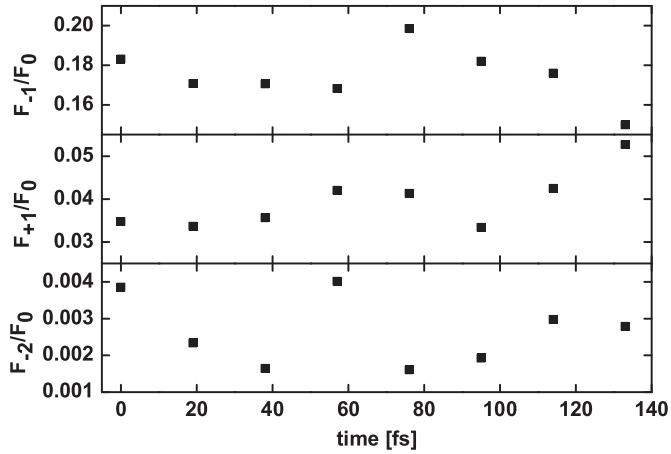

Figure 4.5: *Values of $F_m(\boldsymbol{k})$, normalized with respect to $F_0(\boldsymbol{k})$, for different time steps of the delay line. No clear trend is observable for any F_m. On the timescales in the experiment, Bloch harmonics do not redistribute energy.*

4.4.2 Mode profile of different harmonics

By Fourier analysis and filtering of the optical information, details of the spatial distribution of the individual Bloch harmonics has been obtained. Hereto, the full 2D Fourier transform is multiplied with a window function (width of $0.2\ \pi/a$) containing only one harmonic. Transforming the result back to real space reveals the spatial distribution of that single Bloch harmonic in 2D. This way it is possible to study differences in mode profile of the different harmonics, which has previously been shown for photonic Bloch harmonics [55]. However, by including the available time information we can investigate the evolution of the different harmonics in time. Selecting only the harmonic close to $+\pi/a$, or $m = 0$, and Fourier transforming this back to real space reveals the evolution of the fundamental harmonic as shown in figure 4.6. For the chosen frequency and considering the low interaction strength of the grating, the wavevector of the SPP-mode in the entrance guide turns out to be equal to the wavevector of the $m = 0$ harmonic of the Bloch mode in the grating. For the measurements an excitation wavelength of 1500 nm is used and the time between two frames is 17 fs. Colors are normalized to the maximum in each frame. In the top figure the topography of the grating is depicted. Comparing the different measurement frames in this figure to the frame shown in figure 4.1(b), the

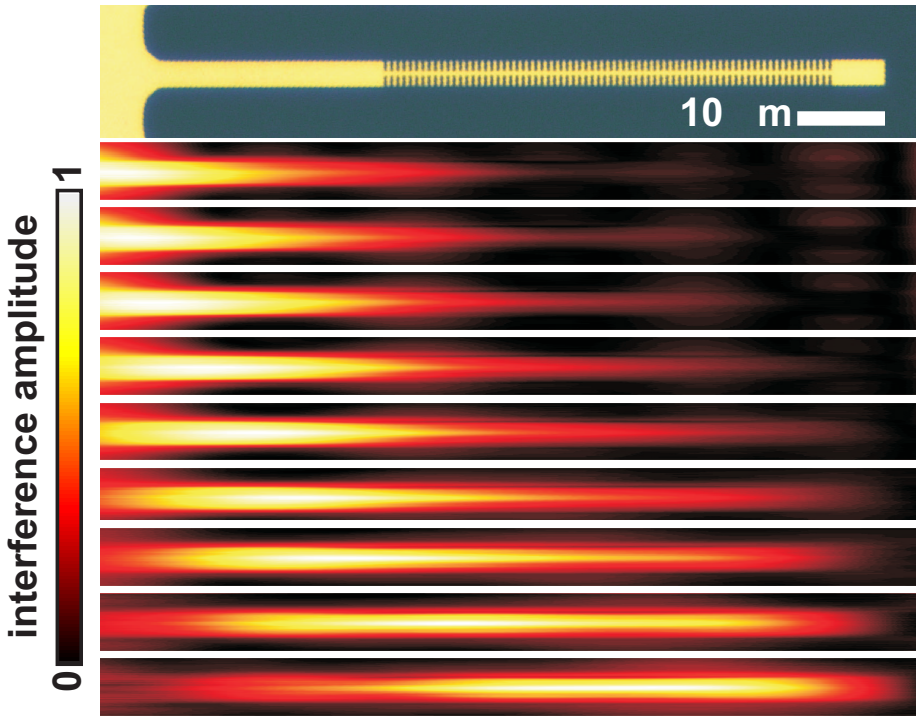

Figure 4.6: *In the top figure the topography of the sample is shown. In the frames below the evolution of the $m = 0$ Bloch harmonic and the SPPs in the entrance guide in real space. Time between two frames is 17 fs, time progresses in the sequence of frames from top to bottom. The excitation wavelength of the SPP wavepacket is 1500 nm. Colors are normalized to the maximum value in each frame. Above the entrance guide already signal is observable which is the fundamental SPP wavepacket having the same wavevector as the Bloch harmonic. Along the grating the $m = 0$ Bloch harmonic has a maximum above the guide in between the corrugations and it moves in time along the grating from left to right.*

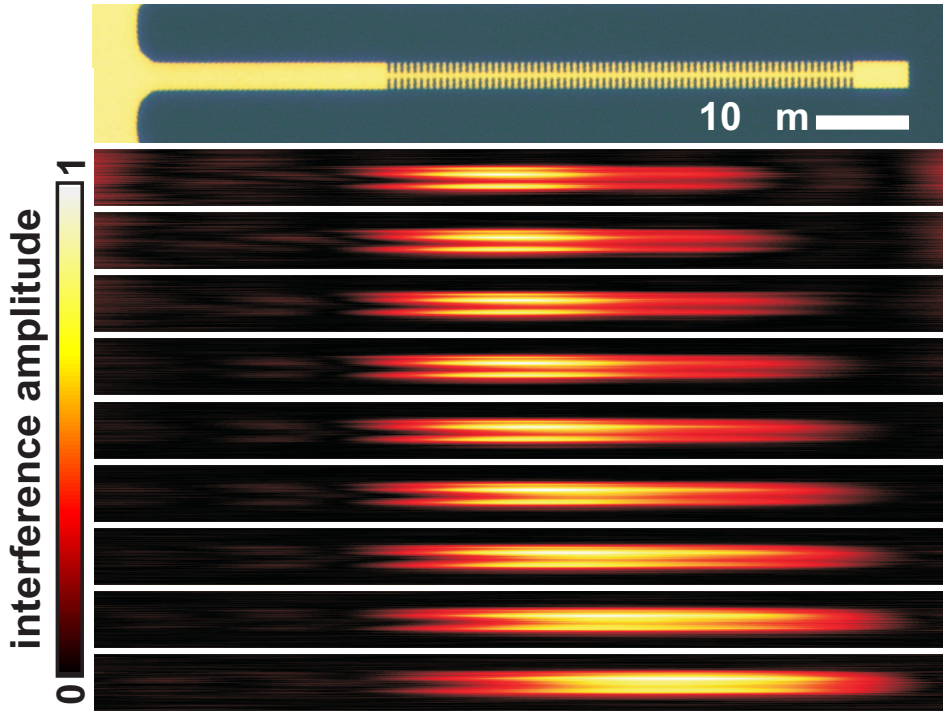

Figure 4.7: *In the top figure the topography of the sample is shown. In the frames below the evolution of the $m = +1$ Bloch harmonic and the SPPs in the entrance guide in real space. Time between two frames is 17 fs, time progresses in the sequence of frames from top to bottom. The first frame corresponds to the same time as the first frame in figure 4.6, same for all succeeding frames. The excitation wavelength of the SPP wavepacket is 1500 nm. Colors are normalized to the maximum value in each frame. This harmonic has its maximum in amplitude above the corrugations and propagates from left to right as part of the Bloch mode propagating in that direction.*

first thing to notice is the absence of interference effects. The standing wave pattern in the entrance guide is no longer visible because the reflected SPPs are filtered out, this way, only the SPPs with a positive phase velocity are left. Also the oscillations having the grating period along the grating have vanished as the periodic amplitude modulation requires the coherent sum of all the Bloch harmonics.

As a comparison, figure 4.7 shows the evolution of the $m = +1$ Bloch harmonic in time as obtained from the same measurement that yielded figure 4.6. Time between two succeeding frames is 17 fs and the excitation wavelength is 1500 nm. Because the data in figure 4.7 come from the same measurement as the data shown in figure 4.6, all frames from top to bottom are measured for the same settings of the delay line as the frames shown in figure 4.6. It appears as the $m = 1$ harmonic in the first time frames has propagated further into the structure as the $m = 0$ harmonic. However, the appeared lead of the $m = +1$ harmonic is a consequence of the normalization to the maximum intensity within each measurement frame. The $m = +1$ harmonic is only present above the grating and the guide in the middle of the grating and not above the entrance guide. Its lateral mode profile does not change in time and has maxima above the grating. This is in contrast to the $m = 0$ harmonic which had its maximum above the guide. Also the mode seems to be slightly asymmetric in the direction perpendicular to the propagation direction. We observe a slightly higher amplitude in the upper half of the graph, then in the lower half. This break of symmetry could be explained by a small tilt of the near-field probe with respect to the sample surface. An other explanation could be topographical artifacts [68].

4.4.3 $F(\mathbf{k})$ for the different harmonics

Repeating the experiments described above for different excitation wavelength yields $F_m(\mathbf{k})$ for different wavevectors. For every excitation wavelength measurements are performed for multiple time steps. As is visible in figure 4.5, the relative strength of the different harmonics does not vary in time and therefore collecting information from the multiple time frames can be used to enhance the signal to noise ratio. Figure 4.8 shows $F_m(\mathbf{k})$ for different excitation wavelength of the Bloch mode, normalized to $F_0(\mathbf{k})$. Error bars are the standard deviation resulting from statistics. The values of $F(\mathbf{k} = -4.2 \cdot 10^{-3})$ are corrected for reflections as was shown in section 4.4.1, which yields $F_{-1}(\mathbf{k})$. From symmetry arguments it is expected that $m = -1$ and $m = +1$ are equal, which is not the case in the measurements, as can be seen in figure 4.8. Apparently, our tip is more sensitive to harmonic $m = -1$, likely because of a small tilt of the probe. Also the $m = -2$ and $m = +2$ are not symmetric,

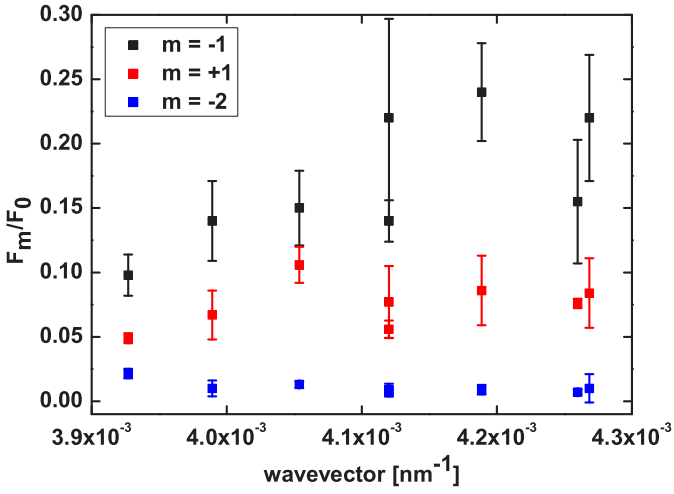

Figure 4.8: *$F_m(\mathbf{k})$ of the different Bloch harmonics normalized to harmonic $n = 0$. Error bars are the standard deviation coming from averaging over multiple time frames.*

as $m = -2$ is measurable, and $m = +2$ is not. The $m = -2$ peak is one order of magnitude smaller that the $m = -1$ and $m = +1$ harmonic. It is important to realize here that the absolute value of the $m = -1$ and $m = +1$ harmonic is different. We will come back to this in section 4.6.

4.5 Theoretical values of harmonic strength

Given the measured $F_m(\mathbf{k})$, it is possible to extract $A_m(\mathbf{k})$ once calculated values of $C_m(\mathbf{k})$ are known. To calculate $C_m(\mathbf{k})$ we use a model proposed by Russell for photonic crystals [59]. For this coupled-wave model we assume an effective dielectric constant of the periodic medium:

$$\epsilon = \epsilon_0[1 + Mcos(\mathbf{K} \cdot \mathbf{r})], \tag{4.5}$$

where ϵ_0 is the effective, average value of the dielectric constant of the waveguide mode and M the modulation depth. Since we know from the experiments that decay is not preventing the Bloch mode to form along the entire grating, decay is disregarded. Note that if M goes to zero i.e., we are left with a unperturbed waveguide, only the fundamental, $m = 0$ spatial harmonic will remain and we are

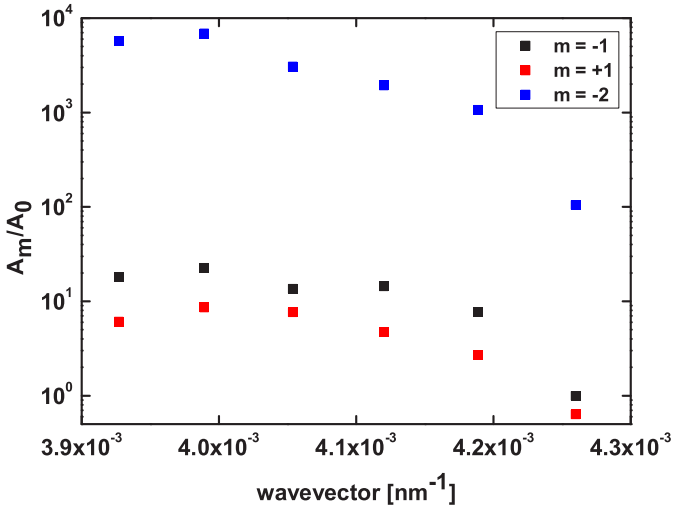

Figure 4.9: *$A_m(\mathbf{k})/A_0(\mathbf{k})$ for the Bloch harmonics $m = 1$, $m = -1$ and $m = -2$, all normalized to harmonic $m = 0$.*

left with an ordinary plane wave in the waveguide. We know from the experiments presented in chapter 5 that $M = 30$ mm^{-1} for our SPP grating. The simplest self-sufficient electromagnetic wave that can exist in such a medium is the Bloch wave as was given in eq. 4.1. From the coupled-wave model it follows that the modulation strength M and optical frequency, contained in $\mathbf{k}$, determine $C_m(\mathbf{k})$.

Substituting eq. 4.1 and eq. 4.5 into the two-dimensional scalar wave equation (i.e., $\partial/\partial z = 0$) [69] gives:

$$(k^2 - \mathbf{k}_m^2)C_m + (M/2)k^2\{C_{m-1} + C_{m+1}\} = 0. \tag{4.6}$$

in which $k = \omega/v_\phi$, where v_ϕ is the average phase velocity of light in the grating. In the experiment values larger than $-3\pi/a < \mathbf{k} < 3\pi/a$ are not observed. We therefore limit calculations to $-2 \leq m \leq +1$. The resulting system of linear equations can be solved with respect to an arbitrary $C_{-2}(\mathbf{k})$. Solving the equations and normalizing to the $m = 0$ harmonic yields the normalized values for $C_m(\mathbf{k})$.

4.6 Different coupling efficiencies for different harmonics

Since we only know relative values for $F_m(\mathbf{k})$ and calculate only the relative values for $C_m(\mathbf{k})$, it is impossible to set absolute values to $A_m(\mathbf{k})$. Therefore we determine the value of $A_m(\mathbf{k})/A_0(\mathbf{k})$, which reflects the relative coupling efficiency for the different harmonics. Figure 4.9 depicts the relative coupling efficiency for different excitation wavelength. It is clear that $A_m(\mathbf{k})/A_0(\mathbf{k})$ depends on m and excitation wavelength. The figure shows that harmonics $m = -1$ and $m = +1$ couple five times up to one order of magnitude better to the probe than $m = 0$ for wavevectors up to $\mathbf{k} = 4.5 \cdot 10^{-3}$ nm^{-1}. The coupling of the $m = -2$ harmonic for low wavevectors is four orders of magnitude higher as for the $m = 0$ harmonic, and for larger wavevectors decreases to two orders of magnitude.

The difference in coupling efficiency is understandable if one realizes that different Bloch harmonics have a different wavevector. Different wavevector may couple different to the near-field probe as was shown in ref. [67]. A larger wavevector corresponds to a smaller effective wavelength and therefore a different interaction to the originally subwavelength near-field probe. The difference between $m = 1$ and $m = -1$, is surprising. As noted before, the harmonics do not have the same absolute wavevector. However, the $m = -1$ harmonic has a smaller absolute wavevector than the $m = +1$ harmonic, which would result in a less efficient coupling to the probe. We suspect that the difference is caused by the orientation of the probe with respect to the sample. It is possible that the probe was tilted slightly. This tilt could have resulted in the situation in which harmonics with a negative wavevector are directed towards the probe, whereas for harmonics with a positive wavevector the situation is reversed. This is expected to result in different coupling efficiencies.

Figure 4.9 shows that all relative coupling efficiencies display a trend of decaying values for shorter excitation wavelength. In the coupled-wave model for frequencies near the stopgap, situated around $4.26 \cdot 10^{-3}$ nm^{-1}, C_0 increases rapidly with respect to all other C_m. However, in the measurements no pronounced increase in $F_m(\mathbf{k})$ is present near the stopgap. We can explain this by taking into account the bandwidth of the wavepackets, which is around 30 nm. Because of this large bandwidth, the measured values represented in the figures for a discrete wavevector, will be an average value over multiple wavevectors. Close to the stopgap, frequencies within the wavepacket that are at the red side of the stopgap will leak out of the grating since they are positioned above the lightline. The loss of frequencies results in an effective blue shift of the wavepacket spectrum, which results in an lower measured $F_m(\mathbf{k})$.

4.7 Conclusions

We have shown for the first time the evolution of individual SPP Bloch harmonics in space and time. The different harmonics, present in one Bloch mode are separated by Fourier analysis and turn out to have different mode profiles. Also we showed that higher order harmonics couple more efficient to a near-field probe then lower order harmonics. The $m = -2$ harmonic couples ion average three order of magnitude better then the $m = 0$ harmonic. This is important to realize because near-field microscopy is the only measurement technique available to study bound, optical Bloch modes. Especially when the amplitude of the different harmonics is used for example to determine extremely small variations in the refractive index [33], one should take to in account coupling efficiencies.

Chapter 5

Slow guided surface plasmons at telecom frequencies

Besides the fundamental interest, slow light has applications in telecommunication [70]. It has been noted that the relevant measure for applying a slow light device is its bandwidth, range of tunability and compactness rather than the absolute slowdown [71]. Slowdown is achieved with three main methods. Firstly, quantum interference effects [72–77] can slowdown light to several m/s, albeit in a very narrow bandwidth. Secondly, photonic crystals [78–80] achieve large bandwidths, but the slowdown factors are much less than in [72–77]. A third method uses stimulated Brillouin or Raman scattering [81, 82]. Surface plasmon polaritons (SPPs) can beat the diffraction limit on chip [6–8, 11]. Recent advances in increasing SPP propagation lengths [11] and the feasibility of all-optical tunability [50], have sparked a huge research effort. In this chapter we report the local observation of slow femtosecond SPP wavepackets. In a highly compact (55 mm) plasmonic structure, we achieve an effective slowdown by a factor of 2 for a bandwidth of 4 THz.

5.1 Introduction

Although it seems counter-intuitive, slowing down light is expected to speed up all-optical data processing [70]. The reason is that inside an all-optical device, light has to be switched light with light itself, which requires optical nonlinearities. These nonlinear effects can be enhanced by using slow light: a device in which the group velocity of light is a factor c/v_g slower (also called group index), where c is the speed of light in vacuum and v_g the group velocity, can be a factor c/v_g smaller in size to obtain the same nonlinear effects. Also one needs c/v_g less power to operate the device [16]. As mentioned before, periodic structures that make use of Bragg scattering, such as photonic crystals (PhCs), can achieve a low v_g over an excellent high-bandwidth. For the proper geometry, Bragg structures exhibit stopgaps, a range of frequencies that cannot propagate in a certain direction. At the edges of this gap, slow modes occur. To slow down the SPP group velocity, a plasmonic Bragg structure, i.e., a plasmonic Bragg grating is needed. The feasibility of this concept has recently been demonstrated in the far infrared for wavelengths between 750 μm and 3 mm (0.1-0.4 THz) [83], but -as a consequence of the low excitation frequency- it required very large structures with a 0.5 mm period. Also, the transmittance of the structure for the slow SPP modes in ref. [83] was only in the order of 0.001 because the structure very effectively scattered SPPs to photons, which were then lost. The possibility has been reported to imbed a waveguide inside a plasmonic Bragg grating, creating a stopgap, and simultaneously maintaining usable propagation lengths for the SPPs by guiding them [51, 84]. Although ohmic losses can never be eliminated completely in plasmonic circuitry, recent progress allows for SPP propagation lengths in the range of mm [51]. Given the ability of plasmonics to break the diffraction limit and miniaturize photonic circuitry, these propagation lengths will allow a high-density of multifunctional plasmonic components to be integrated [11].

5.2 Sample preparation and measurements

To fabricate the structure for slowing down guided SPPs at the desired telecom frequencies, we use e-beam lithography, in combination with lift-off techniques to create the proper features in a 55 nm thick Au film (figure 5.1). More details on the sample fabrication are provided in chapter 3. The structure includes a launch pad (left in figure 5.1) to couple light to SPPs using a Kretschmann-Raether configuration [9]. SPPs are excited at the Au-air interface by a Ti:Sapphire laser pumped optical parametric oscillator (pulse duration 120 fs, repetition rate 80 MHz,

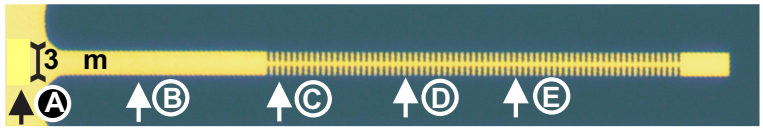

Figure 5.1: *Optical microscope image of the structure under investigation. At the bottom, a SPP launch pad is visible. After the tapered entrance a* 3 μm *wide SPP entrance guide is created. A* 55 μm *long Bragg grating is fabricated in continuation of the entrance guide. The Bragg grating consists of an arrangement of* 1.25 μm *indentations with a period of 750 nm, leaving a 500 nm Au strip remaining at the center. Arrows plus letters indicate measurement positions used in figure 5.2 and figure 5.5.*

wavelength tunable between 1400 nm and 1600 nm, bandwidth 30 nm). After excitation at the launch pad the SPPs enter a 3 μm wide SPP entrance guide via a tapered section. To generate slow SPPs, a 55 μm long Bragg grating is created along the straight guide. The Bragg grating consists of an arrangement of 1.25 μm indentations with a period of 750 nm with a 500 nm Au strip remaining at the center. After the Bragg grating, a small section of unperturbed straight waveguide is continued.

SPP propagation in this structure is investigated with a phase-sensitive and ultrafast near-field microscope [30], optimized for the detection of SPPs. Figure 2.3 shows a schematic of the set-up. The instrument is a combination of a scanning near-field microscope [23] and a Mach-Zehnder type interferometer. A more detailed description of the measurement method is found in chapter 2. The microscope can visualize SPP propagation in time, and in addition is able to obtain local information of the SPP spectral signature.

In order to measure the v_g of the SPP accurately, we fix the position of the near-field probe and scan an optical delay line inside the interferometer. Subsequently we repeat this experiment at equidistant positions along the structure. This way the time-evolution of the SPP-field at fixed positions is obtained as was described in section 2.5.2. Figure 5.2 shows the amplitude of the resulting interferograms at 5 different positions. The first thing to note is that for positions further along the structure, the interferogram shifts to increased delay times, indicating the finite speed of propagation. A few μm after entering the Bragg grating the measured pulse envelope develops in two parts (not yet visible in profile C), each of which can be fitted by a Gaussian envelope. Note that the left part is not an SPP. It is formed by scattered light skimming the sample surface and its speed is exactly equal to c. Only the second pulse shape is formed by the SPP wavepacket. The inset in figure 5.2 shows the two fitted Gaussian shapes. Each of the pulses, the skimming

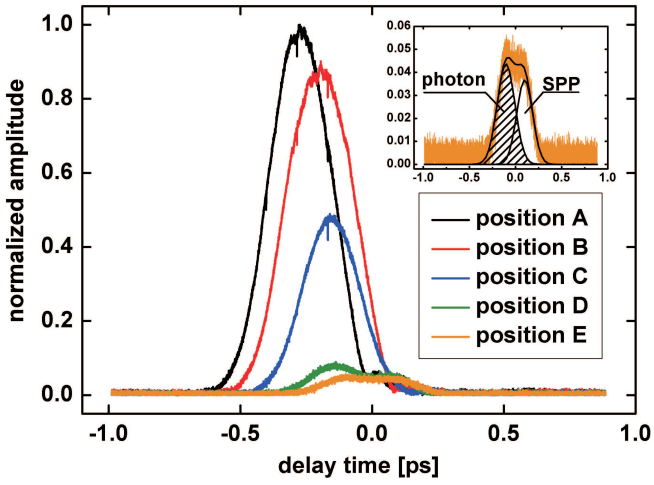

Figure 5.2: Amplitude of the cross-correlation functions of the probed SPP field and the pulse in the reference branch of the interferometric setup. Positions are indicated in figure 5.1. The inset shows the two Gaussians used to determine the speed of the individual pulses. The right wavepacket is assigned to SPPs, whereas the faster wavepacket is associated with photons, launched at the entrance guide-grating interface, and skimming over the surface. Because only the absolute values of the interferogram are shown, the noise level does not fluctuate around zero, whereas the fit does go to zero.

light and the SPP wavepacket retains their Gaussian shape without distortions. In figure 5.3 the position of the slow SPP wavepacket in time is shown for the different measurement positions. As long as the wavepacket is inside the entrance guide, its group velocity is close to c, but as it enters the Bragg grating it slows down to roughly $c/2$. This shows that the Bragg grating slowed down the SPP wavepacket with a factor of 2.

Repeating the experiment for different incident optical frequencies, the SPP group index as a function of incident frequency is measured (blue points in figure 5.4). As the frequency is tuned away from the frequency corresponding to the slow SPPs, the SPP group index decays gradually to the value of a straight SPP waveguide. This observation is consistent with the presence of an SPP stopgap with an edge at 203.4 THz (≙1475 nm) excitation wavelength.

The combined interference amplitude and underlying phase information that is measured, is in fact an E-field cross-correlation function (see figure 5.2 for the am-

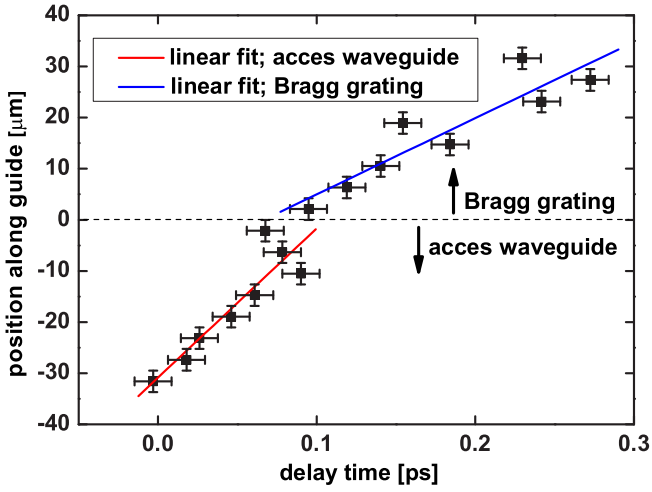

Figure 5.3: *Position of the maximum of the SPP wavepacket in time at different positions along the structure. The transition between entrance guide and Bragg grating is at position 0 μm. From this we obtain the group velocity of the SPP pulse in the entrance guide and in the Bragg grating, which are* $3.04 \cdot 10^8 \pm 0.3 \cdot 10^8$ *m/s and* $1.54 \cdot 10^8 \pm 0.2 \cdot 10^8$ *m/s, respectively.*

plitude information). It contains information on the spectrum of the wavepacket at the position of the probe, since the pulse in the reference branch does not change spectrally. Figure 5.5 shows the spectral signature obtained by Fourier transforming the measured cross-correlation functions for the different positions along the structure for the slowest SPP. In the first section of the guide, i.e., the part without the Bragg grating, only the amplitude of the SPP spectral information changes (not visible in the normalized graphs). From the decay of the amplitude with distance, we determine an amplitude propagation length of 144 ± 5 μm inside the entrance guide. However, as the SPP propagated a few μm inside the Bragg grating, a dip centered around 203.7 THz (≙1473 nm) appears (again not yet visible in measurement C). This is a clear indication of a stopgap at 203.7 THz (≙1473 nm) with an estimated width of 0.4 THz (≙3 nm FWHM). At first sight, it may seem like the depth of the frequency dip shrinks and the spectral information as a whole broadens as the wavepacket propagates deeper into the Bragg grating. The dip appears to decrease because frequencies at the blue side of the stopgap are situated above the light line and therefore couple to photons easily, resulting in extra losses. Also,

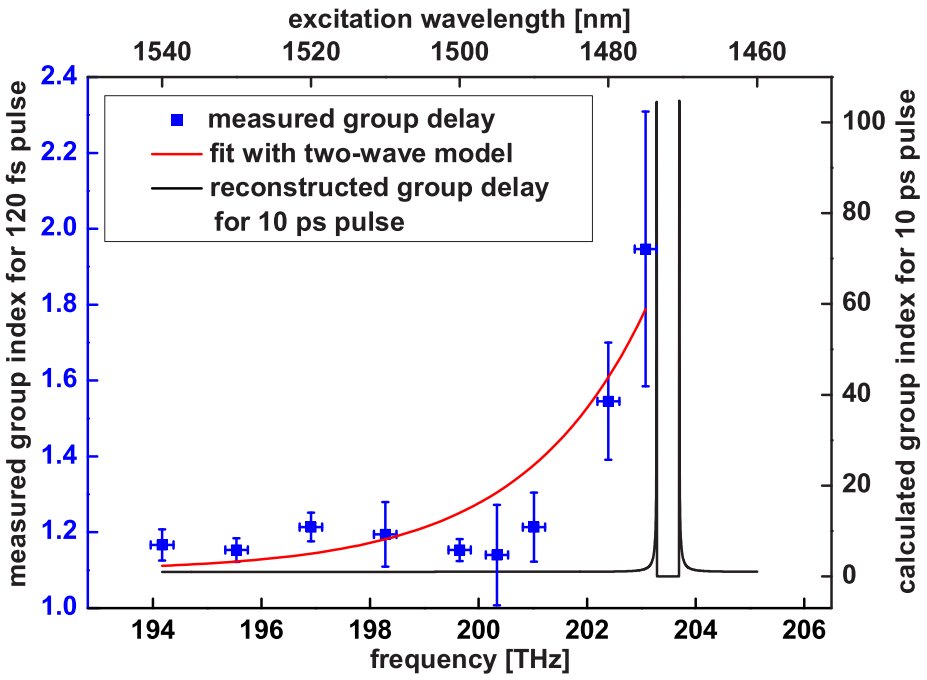

Figure 5.4: Measured and calculated group indices for different SPP excitation frequencies. The measured group delay is shown in blue. The red line indicates the fitted group delay if one takes into account the bandwidth of the pulses used. In black the expected group delay of the structure is shown for an experiment with 10 ps pulses.

since the peak of the SPP spectrum is very close to the stopgap, the peak of the SPP spectrum will decrease with respect to the sides of the spectrum, which appears in the normalized data as a broadening of the spectral information and a reduced depth of the spectral dip due to the stopgap.

5.3 Excluding wavepacket bandwidth

Note that the effective slow down of the wavepacket group velocity is as large as a factor of 2, even though the bandwidth of the pulse (typically around 4 THz or 30 nm FWHM) exceeds the width of the stopgap by an order of magnitude. For a structure as short as 55 μm we found a delay-bandwidth product as large as 1.3. Using 10 ps pulses, rather than the 120 fs used in this investigation, would already suffice for 100 GHz bandwidth telecom applications. A simplified model of the creation of a stopgap, the two-wave approximation [85], is used to evaluate the potential of our structure at 100 GHz bandwidth. This model describes how a stopgap develops due to the two partial waves that couple as a result of the periodic indentations. By fitting the experimentally found group index as a function of frequency, while taking into account the bandwidth of the SPP wavepacket (red line in figure 5.4), we found the strength with which the Bragg grating couples to the SPP modes. The model only describes the data for frequencies at the red side of the stopgap as frequencies at the blue side of the stopgap incur high radiative losses and are therefore not detected. The coupling strength, a measure for the strength of the interaction between a Bragg grating and an E-field, of our Bragg grating turns out to be 30 mm^{-1}. Using this value, we calculated the theoretical group index of the structure for a 10 ps pulse (black line in figure 5.4). It shows that while a group index for 120 fs pulses was experimentally found to be 2 in the experiment, group index as high as 100 are obtainable in the fabricated structure. As a result, all-optical switches in plasmonic structures that exploit, e.g., the Kerr effect [50] will be able to operate with low powers of an external switching laser owing to the slowdown of the SPPs. Our findings therefore open avenues for highly compact photonic components, including low-power highly compact all-optical switches. In addition, we expect that slow SPPs as observed in this letter will increase the sensitivity of biosensors [15, 38] due to the increased SPP-matter interaction of the slow SPP.

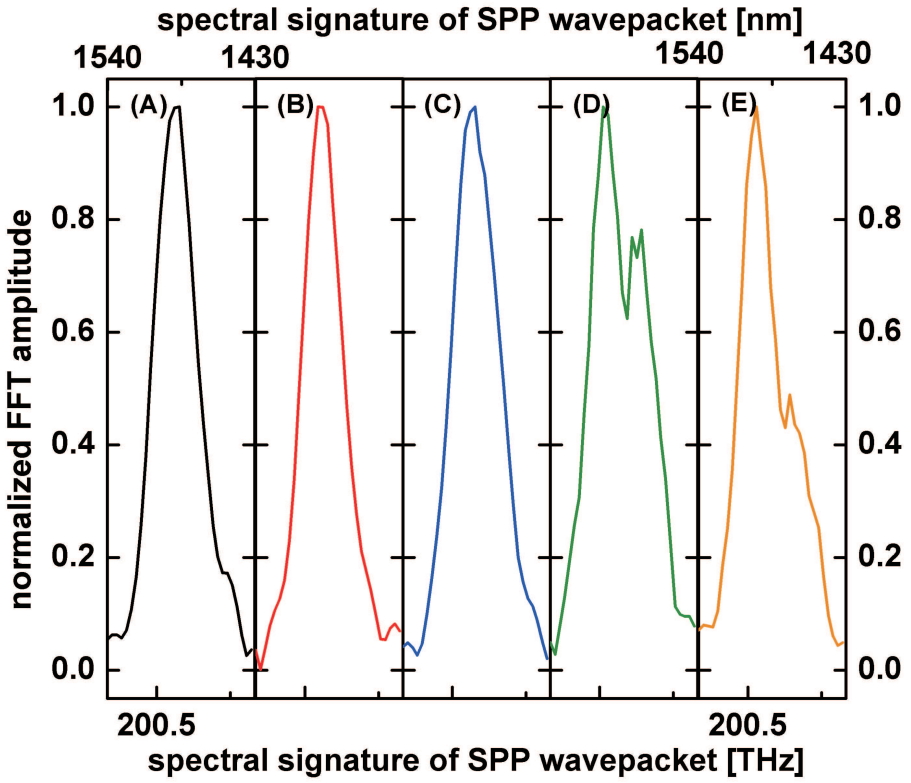

Figure 5.5: *SPP spectral signature at different positions along the structure. Positions A and B are taken along the entrance guide. The straight 3 μm guide has a negligible influence on the propagating SPP spectral information. Profiles C, D end E are taken above the grating and profile D and E show a dip in their spectrum due to the stopgap of the Bragg grating. Profile C is to short after the start of the grating to show any effects. We attribute the broadening of the spectral information as the SPP propagates further along the grating to normalization effects. Because the Bragg grating stopgap is close to the central frequency of the SPP, the center of the SPP spectrum is attenuated faster than the sidebands of the spectrum, resulting in an effective broadening of the normalized spectrum. The decreasing of the depth of the dip when going from D to E is caused by the fact that the Bragg grating stopgap couples frequencies at the blue side of the stopgap to photons, since they are positioned above the light line. Letters indicate positions shown in figure 5.1.*

Chapter 6

Summary and conclusions

This thesis showed the realization of a novel photon scanning tunneling microscope (PSTM) for time-resolved and phase-sensitive measurements on guided surface plasmon polaritons (SPPs). In first instance we investigated a model system that has been described in literature in great detail both theoretically and experimentally: a straight metal SPP guide. After that we studied a Bragg grating to reveal the properties of SPPs in tailor made structures. We were able to visualize SPP propagation in both systems and determined SPP dynamics.

In chapter 2 we explained the measurement setup that was built to perform the measurements reported in this thesis. The reasons for building a novel microscope and its requirements were discussed. A theoretical background on time-resolved and phase-sensitive measurements was given. Finally, the measurements on propagating SPP wavepackets, guided by a straight SPP guide, were presented. The structure was chosen as a reference structure to show that all the requirements for the microscope were met. The presented measurements showed the phase of the SPP E-field and allowed the determination of the SPP phase velocity. Also measurements on the dynamics of SPPs were shown, enabling us to measure the SPP group velocity and propagation length.

To show the added value of phase-resolved measurements, we introduced a Bragg grating along a part of the straight SPP guide that was studied in chapter 2. The impedance mismatch between the grating and straight guide resulted in a reflection back into the guide. These reflections were studied chapter 3. For frequencies within the grating stopgap the reflection was enhanced. The phase-sensitivity allowed the measurement of the complex reflectivity of SPPs. The determination of the phase shift upon reflection gave us the effective position of reflection inside the grating, the phase length. The measured values for the reflection were in good agreement with calculations.

Chapter 4 focussed on SPPs inside the Bragg grating itself. When a wave propagates through a periodic medium, Bloch's theorem has to be obeyed. As a result, a Bloch mode will form, containing multiple spatial Fourier components, the Bloch harmonics. We were able to visualize in time the individual Bloch harmonics that are part of the same Bloch mode. Individual harmonics turned out to have different mode profiles. By comparing the measurements to a theoretical model it was possible to assign different coupling efficiencies between the near-field probe and different Bloch harmonics.

The ultrafast property of the PSTM showed its added value in chapter 5 where we showed that the group velocity of SPP wavepackets propagating along the SPP Bragg grating is reduced. A reduction of the group velocity by a factor of 2 for the full bandwidth of the wavepacket was shown. This lower group velocity was

caused by the opening of a stopgap inside the grating. We also showed that the structure would allow for a group velocity of $c/100$, if the bandwidth would be reduced to 100 GHz instead of the 4 THz used in the experiment.

6.1 Outlook

The research described in this thesis will open new doors in research on SPPs. Numerous (plasmonic) structures can be studied ultrafast and with phase-sensitivity with the newly developed microscope. The PSTM also enables the investigation of photonic structures, like photonic crystals. Also a new fields in optics: that of metamaterials, can be studied with the instrument described in this thesis.

6.1.1 SPPs in passive structures

Straight waveguides and Bragg gratings are only two out of the long list of passive SPP components like bends, splitters, resonators, cavities, directional couplers, and so on. All these structures are necessary for applications of SPPs in for instance telecommunication.

For channel plasmons, SPPs bound to and propagating along, the bottom of a V-shaped groove milled in a metal film, a large gallery of subwavelength components has already been studied using a PSTM [11]. It would be interesting to extend these measurements with ultrafast and phase-sensitive information and see if slow channel SPPs are also achievable. There exists a third class if SPPs: long range SPPs (LRSPPs) [86]. These are SPPs associated with the a symmetric mode coupled to the upper and lower interfaces of a thin metal film embedded in dielectric. LRSPP modes are symmetric in amplitude and have a node in the metal film to reduce losses. LRSPP modes are not accessible for measurements with a PSTM, but extremely important for SPP applications since the propagation length of LRSPPs is in the order of mm.

The toolbox of passive SPP components can be extended by components composed of metal nanoparticles. Arrays of these particles also support SPPs and can be used to construct waveguides [87, 88]. It would be very interesting to investigate the dynamical properties of SPP modes coupling from one metal nanoparticle to the next particle, as well as the phase behavior of a SPP propagating along an array.

6.1.2 SPPs in active structures

A next step towards SPP applications would be to turn to active SPP structures. Modulators and switches operating at telecom wavelengths have already been reported for LRSPPs based on the thermo-optic effect [89]. Optical bistability, modifying the optical properties of a nonlinear material by the use of an (external) light source, can help to switch light with light itself [90]. SPPs are extremely sensitive to their surrounding dielectric environment and can therefore be switched by a relative low power of the switching laser [50]. Our PSTM is an ideal instrument to study active components as it can visualize switching with time scales that are orders of magnitude faster than the switching frequencies that are typical desired, that is GHz up to THz.

6.1.3 Subwavelength hole arrays

Since the discovery of extraordinary transmission through subwavelength hole arrays in 1998 [91] it has been the inspiration for over eight hundred peer-reviewed papers. Extraordinary transmission is extraordinary because the amount of light transmitted through a metal film perforated with subwavelength holes, exceeds the open fraction. In addition to the periodicity and type of metal, also the shape of the subwavelength hole has a huge influence on the amount of transmission and the position of the transmission maxima [92, 93].

The hole arrays are an interesting structure to investigate with our PSTM. Especially since hole arrays potentially can be used as very sensitive sensors [94]. These sensors can be made even more efficient because of the recent discovery that the non-linear properties of hole arrays can be enhanced by slow propagating modes propagating through the holes [95]. However, this slow light hypothesis still has to be verified, and an ultrafast PSTM is a good instrument to do this. Already far-field time-resolved measurements on subwavelength hole arrays are reported [96] and also phase-sensitive studies on hole arrays are reported both theoretical [97] and experimental using a PSTM [98]. The next step would be to combine these two and in addition do this in the near-field.

6.1.4 Metamaterials

Metamaterials can have a negative index of refraction [99]. In literature these materials are also called left-handed materials (LHM). If the index of refraction becomes negative, the counter intuitive effect occurs that a ray of light entering a material from air will refract away from the normal instead of towards the normal.

Inside a LHM the phase and group velocity will be negative as was experimentally demonstrated [100]. A negative phase and group velocity imposes a negative time delay if a light pulse propagates trough a LHM. This means that a light pulse will exit the LHM before it enters the material. Time-resolved measurements already showed that a pulse indeed seems to exit the structure before it enters [100], but visualizing this using a PSTM would be a unique experiment.

Besides the fundamental interest in a negative index of refraction, it was proposed that these materials can be used to obtain a perfect lens [101, 102], which was also shown to work in the laboratory [103]. A perfect lens is "perfect" because it will also image the exponentially decaying evanescent waves (e.g., SPPs). Maintaining these modes enables the reconstruction of an object with a resolution beyond the diffraction limit. Very recently two groups showed simultaneously, but with a slightly different approach, that alternating layers of different materials can image subwavelength features in the far-field [104, 105]. In the approach by Smolyaninov *et al*. [105] SPP rays magnify subwavelength features as the rays diverge due to rings of poly(methyl methacrylate) PMMA.

Recently it was also proposed that properly designed metamaterials could bend light around an object without disturbing it and thus act as a cloak [106]. For this idea to work, a prescribed spatial variation of the electrical permittivity and magnetic permeability should be introduced in the cloak. Light rays tends to take the shortest route between two points, which is normally a straight line. As the material properties of the cloak are carefully designed, the quickest path can be one that bends around an object. Ultimately the cloak will have no reflections and shadow. A few moths after the theoretical prediction, it was shown that this idea works in the laboratory for microwave frequencies [107]. Although the cloak worked for only one polarization and a limiting frequency range, it was possible to hide a copper cylinder reasonably well and prove that the concept also works in practice. It would be a beautiful experiment to visualize the E-fields as they are diverted around the cloak.

6.1.5 Photonic crystals

A very hot topic in optics for the last decade is the field of photonic crystal (PhC), or photonic bandgap (PBG) devices. These devices posses the ability to steer, and switch light on a nanometer scale [5, 78]. PhC's are composites of periodically alternating dielectric properties, in which the periodicity is in the order of the wavelength of the light. The periodic variations in material properties gives rise to a range of frequencies of light that is forbidden to propagate through the material.

As such, PhC's provide a similar control over the propagation of light as semiconductors do in the case of electrons. Therefore, optical interconnects at the size of electrical interconnects become within reach.

PhC's are already examined in great detail with an equivalent PSTM as described in this thesis [55, 79]. Nevertheless, these studies only mark the beginning of the near-field research of PhC's. For instance, active photonic crystal devices like introduced in ref. [80] are very interesting to study time-resolved.

Samenvatting voor allen

Je drukt op je toetsenbord op de letter A, en er verschijnt een A op het beeldscherm. Toch perst zich geen fysieke letter A door de kabel die aan het toetsenbord vast zit naar de PC. Er gaat een elektrisch stroompje door de kabel, die de PC interpreteert, en doorstuurt naar het beeldscherm, opnieuw in de vorm van een stroompje. Tot slot zet het beeldscherm het stroompje om in een letter op het scherm.

Alle informatie in een PC, maar ook in een MP3-speler, DVD-speler of digitale camera, reist in de vorm van kleine elektrische stroompjes. Al die stroompjes worden gestuurd door schakelaars (transistoren). Dit proces werkt tot nu toe uitstekend. Maar, snellere PC's of meer geheugen in een MP3-speler, betekent meer transistoren, in idealiter minder volume, want alles moet klein en compact. Het einde van de groei van steeds snellere PC's en MP3-spelers met steeds meer geheugen komt in zicht. In de nieuwste computer chips zitten miljoenen transistoren van 30 nanometer (30 miljoenste millimeter) zo dicht mogelijk op elkaar gepakt. Als de transistoren kleiner blijven worden, zullen binnenkort onderdelen in de transistor kleiner moeten worden dan één molecuul. En dat is toch wel een serieuze limiet. Bovendien zorgen alle stroompjes in de PC voor opwarming. Als de draadjes tussen PC onderdelen blijven krimpen, warmen ze in de nabije toekomst zelf zoveel op dat ze licht gaan uitzenden: het worden gloeilampjes! Niet voor niets zit er een grote ventilator in elke PC en krijg je een lekker warme schoot van je laptop.

Een oplossing voor de naderende problemen is om alle elektrische stroompjes te vervangen voor licht. Licht kan ook informatie vervoeren, zoals nu al gebeurt in glasvezel kabels. En dit kan extreem efficiënt: al het internet verkeer tussen Amerika en Europa gaat door glasvezelkabels, en internet via de glasvezel kan veel meer informatie per seconde verwerken dan de oude telefoonlijn. Het grote

voordeel van licht is dat er zoveel verschillende kleuren zijn als je maar kan verzinnen. Elke kleur kan andere informatie bevatten, en vervolgens gaan alle kleuren tegelijk door dezelfde glasvezelkabel zonder dat ze elkaar storen. Maar hoewel licht al snel 1000 maal meer informatie kan versturen dan elektrische stroom, is een glasvezel ook al snel 1000 keer dikker dan een stroomdraadje. Maak je de glasvezel dunner dan lekt het licht eruit. En we wilden juist kleine chips maken.

Wellicht zijn de voordelen van elektronische schakelingen: klein, en die van licht: veel informatie tegelijkertijd, te combineren dankzij plasmonen. Een plasmon is licht dat als het ware zit vastgeplakt aan een metaal. Zo behoudt een plasmon de voordelen van licht, namelijk dat het uit verschillende kleuren kan bestaan, en tegelijkertijd kan het reizen langs de kleine metalen draadjes die nu ook al in elke PC zitten. In het dagelijks leven zien we plasmonen al regelmatig. Glas in lood heeft zo'n mooie heldere kleur omdat er in het glas kleine metalen bolletjes zitten. Klein betekent in dit geval enkele tientallen nanometer en dus niet zichtbaar met het blote oog. Op deze bolletjes ontstaan plasmonen, en de grote van het bolletje bepaalt de kleur van het plasmon. Andere formaten bolletjes, of andere materialen zorgen voor andere kleuren plasmonen en dus een andere kleur glas.

Tot nu toe is de kennis van plasmonen veel minder dan voor "gewoon" licht. Zo is nog nooit gemeten hoe snel een plasmon nou eigenlijk over een metalen draadje beweegt. Met de lichtsnelheid? En hoewel verschillende wetenschappers al aantoonde dat je "gewoon" licht langzamer kan laten reizen, is ook dit voor plasmonen nog nooit gedaan (althans niet voor kleuren die nuttig zijn voor datatransport). Vertragen van licht is belangrijk omdat dat het begin vormt van het meest ultieme geval: licht of een plasmon echt stil zetten. Als je licht of een plasmon stil zet, is het te gebruiken als geheugen. Laat een plasmon bijvoorbeeld de zin bevatten die je net hebt "geknipt" uit je tekst, en zet dat plasmon stil, totdat je op "plakken" drukt. Dan mag het plasmon weer bewegen en de zin naar het beeldscherm sturen.

Een andere toepassing van langzame plasmonen is bij het detecteren van stoffen zoals drugs of bio-moleculen die bij bepaalde ziektes horen. Er bestaan al commerciële apparaten die bepaalde ziektes detecteren in iemands bloed door gebruik te maken van plasmonen. Als een plasmon nu twee keer zo langzaam door dit apparaat gaat, heeft het twee maal zoveel tijd om de belangrijke moleculen te identificeren, en dat maakt het apparaat twee maal zo gevoelig.

Mijn promotieopdracht was: meet hoe (snel) plasmonen zich voortbewegen, en probeer deze snelheid langzamer te maken. Het eerste waar je dan tegenaan loopt is dat er geen apparaat bestaat om de snelheid van een plasmon te meten. Dus zo'n apparaat moest ik eerst bouwen. Als voorbeeld hadden we een aan de

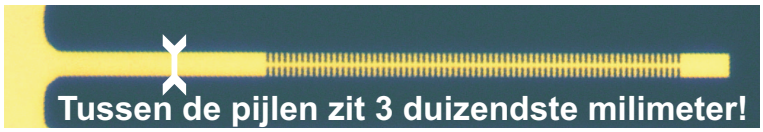

Figure 6.1: *Een microscoop plaatje van een gekarteld gouddraadje. Het geel gekleurde stuk is een goud laagje van 55 nanometer dik en de draad is 3 micrometer breed, dit is het stuk tussen de witte pijlen. Blauw/grijs is het glas waar het goud op ligt. We maken plasmonen aan de linkerkant van het plaatje en deze reizen naar rechts over de draad. Onderweg moeten ze langs een stuk met kartels, waar de plasmonen afremmen.*

Universiteit Twente ontwikkelde microscoop waarmee de snelheid van licht al was gemeten. Het idee van de microscoop is als volgt: maak aan het einde van een glasfiber een heel scherp puntje, van 200 nanometer. Breng dit puntje vervolgens tot ongeveer 10 nanometer boven een plasmon en dan "zuigt" de glasfiber een beetje van het vastgeplakte licht weg. Het opgezogen plasmon wordt in de glasfiber weer omgezet in gewoon licht en door de glasfiber naar een meetpunt gebracht. Dit licht vergelijk je met licht dat door lucht reist, en waarvan je weet hoe snel het gaat. Komt het licht door de lucht eerder aan bij het meetpunt dan het licht uit de glasfiber, dan was het licht door de lucht sneller. Hoeveel eerder het licht door de lucht aankomt, bepaalt hoeveel sneller het was. Op deze manier bepaal je of het plasmon even snel, sneller of langzamer gaat dan licht in lucht.

Na twee jaar bouwen is het gelukt om een microscoop te maken die kan meten hoe snel een plasmon reist en in hoofdstuk 2 van dit proefschrift beschrijf ik hoe de microscoop werkt. Verder beschrijf ik de meting waarin we zien dat plasmonen die vastgeplakt zitten aan een gouddraad van 6 micrometer breed (6 duizendste millimeter) bijna net zo snel gaan als licht in lucht. Ze reizen met ruim $4/5^{e}$ van de lichtsnelheid.

Kunnen die plasmonen nog langzamer? Hiervoor maakten we een goud draad van 3 micrometer breed met langs een deel van de draad een kartelrand aan beide zijden, zie figuur 6.1. Het smalle deel tussen de kartels vormt een blokkade voor het plasmon. Iedere blokkade kaatst een deel van het plasmon terug (het werkt deels als een spiegel), en laat een deel door. Door een hele reeks blokkades te maken krijg je iets dat lijkt op "drie stappen naar voren, twee terug." Hoe beter de afstand tussen de ribbels is geoptimaliseerd, hoe meer stappen terug en minder stappen naar voren het plasmon zet. Op deze manier duurt het langer voordat het plasmon bij de laatste kartel komt, en is hij dus langzamer gegaan, dan wanneer er geen kartels waren.

In hoofdstuk 5 beschrijf ik de metingen aan de gouddraad met kartels. Het

blijkt dat de plasmonen twee keer zo langzaam gaan als licht in lucht. Met andere woorden, het zette steeds twee stappen van links naar rechts, en daarna weer één terug. Op deze manier gaat het twee keer zo langzaam. Dit betekent dat als onze goud structuur wordt geïntegreerd in bestaande commerciële apparaten, deze bepaalde ziekten twee maal zo gevoelig kunnen opsporen als dat zij op dit moment doen!

De overige hoofdstukken van dit proefschrift gaan in meer detail in op de precieze eigenschappen van de kartels en de plasmonen. In hoofdstuk 3 ga ik dieper in op de spiegeleigenschappen van de kartels. Het blijkt dat de kartels sommige kleuren plasmonen beter spiegelen dan andere kleuren, en dit verklaren we met een theoretisch model. Deze vinding sluit goed aan bij de metingen van de plasmon snelheid. De kleuren die het beste reflecteren geven ook de langzaamste plasmonen. In hoofdstuk 4 bestuderen we hoe het plasmon de vorm van de kartels overneemt en zelf een "geribbelde vorm" krijgt.

Kan ik straks een complete film in één minuut downloaden of de ventilator uit mijn PC halen omdat het mogelijk is om plasmonen langzamer te laten reizen? De komende tien jaar zeker niet. Maar als je je bedenkt dat een computer nog niet zo lang geleden net zo groot was als een complete kamer en minder functies had dan je huidige mobiele telefoon, dan weet je maar nooit. De gebouwde microscoop is voorlopig uniek in de wereld en continu in gebruik. Naast onderzoek aan plasmonen is de microscoop ook te gebruiken voor het onderzoek aan licht in bijna alle denkbare toepassingen. Dus al zitten langzame plasmonen voorlopig niet in een PC, de inspanning om ze te vinden heeft nu al zijn nut bewezen.

Samenvatting

Voortgedreven door de “self-fulfilling prophecy”, de wet van Moore, moeten computerchips in de toekomst kleiner en sneller blijven worden. Naast anderen, doemen twee serieuze barrières op: de beperkte bandbreedte die haalbaar is met elektronica en warmtedissipatie/energieverbruik. De introductie van optica in de chips vormt een mogelijke oplossing voor deze problemen. Signaaltransport met behulp van licht kan met een veel grotere bandbreedte dan met elektronica. Ook hebben optische componenten niet het nadeel dat veel van de energie tijdens datatransport verloren gaat in de vorm van warmte. Behalve dat warmte een bron van energieverlies is, begint het ook het ook een serieus probleem te worden voor het goed functioneren van ultrasnelle elektronische chips.

Het klinkt tegen intuïtief, maar voor snellere optische chips is langzaam licht (een lage groepssnelheid) wenselijk. Een optische router bijvoorbeeld schakelt licht, maar synchroniseert het ook. Voor de synchronisatie moet het licht even in de wacht staan. Wellicht nog belangrijker: langzaam licht heeft een grotere, effectieve licht-materie interactie. Dit maakt schakelen makkelijker en mogelijk met minder energie. Nadeel van conventionele optica is dat de diffractielimiet grenzen stelt aan hoe klein een fotonische component kan worden. Maar optica op een nanometer schaal is weldegelijk mogelijk door gebruik te maken van oppervlakte plasmon polaritonen (SPPs). Langzame SPPs vormen een krachtig ingrediënt dat nodig is op de weg naar plasmonische toepassingen in PC’s en telecom. Maar het verlagen van de groepssnelheid van SPPs vereist nieuwe nanostructuren. Verder is een instrument nodig om op een nanoschaal de SPP groepssnelheid te meten.

SPPs zijn de oplossing van Maxwell’s vergelijkingen voor het grensvlak tussen een metaal en een dielectricum (meestal lucht). Deze oplossing is een gebonden en lopende oppervlaktegolf. Anders gezegd: een SPP is een resonante interactie

tussen licht en de vrije elektronen aan een metaaloppervlak. SPPs hebben een grotere golfvector (kleinere golflengte) dan fotonen met dezelfde frequentie. Dit heeft als voordeel dat ze gebruikt kunnen worden in componenten op een schaal kleiner dan de golflengte van het licht met dezelfde frequentie. Deze grotere golfvector maakt dat SPPs aan een lucht-metaaloppervlak niet zijn aan te slaan met licht dat door lucht aankomt. Daarom laten we laserlicht door het glassubstraat op de onderkant van de te onderzoeken structuur vallen. Door nu de hoek van inval aan te passen wordt de golfvector van de SPPs gelijk aan de golfvector van de fotonen parallel aan de goud film. Onder de totale interne reflectie conditie van het glassubstraat bereikt een fractie van het evanescente veld van de laser het goud-luchtgrensvlak en kan je hier SPPs aanslaan.

Eenmaal aangeslagen is een SPP niet meer te bestuderen met een conventionele microscoop. SPPs zijn wel te bestuderen met een photon scanning tunneling-microscoop (PSTM). Een PSTM gebruikt een nabije-veld probe, een glasvezel die eindigt in een puntje van typisch 200 nm in diameter, in plaats van een lens. Als de probe in het evanescente veld van een SPP wordt gebracht, koppelt een klein deel van dit veld naar de probe waar het als een lopende golf in de glasvezel verder gaat naar een detector. De grootte en vorm van de probe bepaalt de resolutie van de meting en is subgolflengte.

Deze techniek is uit te breiden voor het doen van tijdsopgeloste en fasegevoelige metingen [26–32]. Hiervoor laten we het opgepikte licht interfereren met licht uit een referentiearm met een constante optische lengte, maar met een 40 kHz verschoven optische frequentie. De interferentie van het licht uit de referentie arm en het opgepikte SPP E-veld geeft een zweving in de tijd door het verschil in frequentie. Een lock-in detector die alleen naar de zweving kijkt, bepaalt vervolgens de fase van het signaal. Tijdsopgeloste metingen doen we door een gepulste femtoseconde laser te gebruiken. De mate van tijdsoverlap tussen de referentiepuls en de opgepikte puls op het punt van samenvoegen, bepaalt de sterkte van de interferentie tussen de referentiearm en het opgepikte SPP veld.

Fotonische structuren zoals golfgeleiders en fotonische kristallen zijn met de beschreven techniek al uitgebreid bestudeerd. SPPs daarentegen zijn al wel onderzocht met een PSTM [24, 36], maar nog nooit fasegevoelig of tijdsopgelost. Deze papers bestuderen rechte SPP geleiders van enkele μm breed. Wij fabriceerden vergelijkbare geleiders als referentiestructuren om aan te tonen dat we de groepssnelheid van SPPs kunnen meten. Het resultaat is te zien in figuur 6.2. Figuur 6.2(a) toont de topografie van de SPP geleider gemeten met de hoogte terugregeling van de probe. De geleider is van goud en 55 nm dik, 80 μm lang en 6 μm breed. SPPs slaan we aan aan het begin van de geleider, onderin de

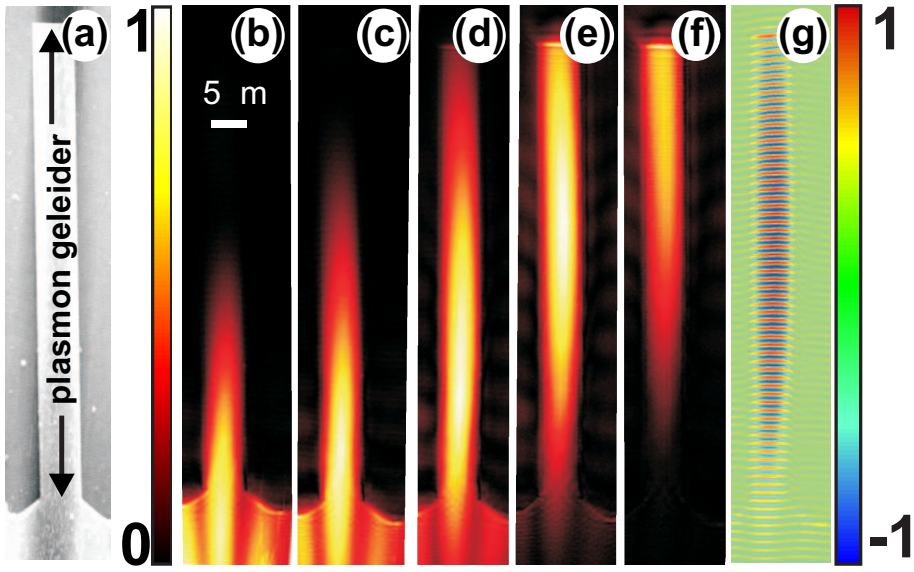

Figure 6.2: *(a): Gemeten topografie van de SPP geleider, verkregen met de hoogte terugkoppeling van de PSTM tegelijkertijd met de optische metingen. De geleider bestaat uit een 55 nm dikke Au-laag op een glassubstraat, en is* 6 *µm breed en* 80 *µm lang. SPPs worden aangeslagen met een fs-laser (golflengte in lucht: 1500 nm) aan de onderkant van de figuur (b). In (b) t/m (f) tonen we de amplitude van het opgepikte elektrisch veld van een SPP, gemeten met de PSTM. Tussen de frames is elke keer de referentiearm langer gemaakt zodat de referentiepuls 48 fs langer onderweg is. Hierdoor interfereert de referentiepuls met SPPs die ook langer onderweg zijn, en dus verder langs de geleider hebben gereisd. In (g) is het volledige ruwe meetsignaal van frame (e) te zien. We meten niet alleen de amplitude van het SPP E-veld, maar ook de fase. Individuele fase fronten zijn duidelijk zichtbaar als lijnen haaks op de geleider.*

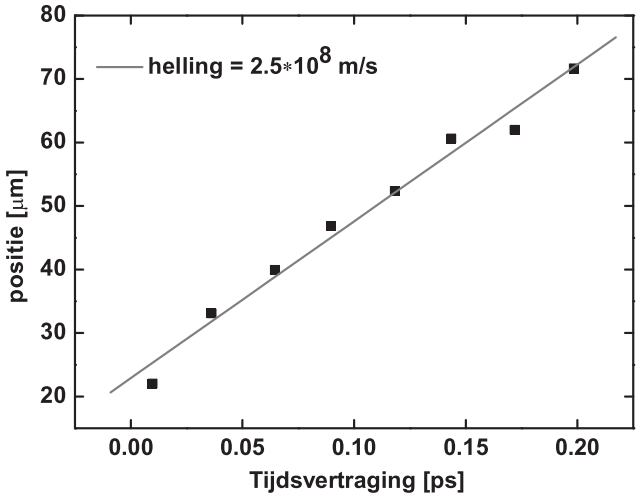

Figure 6.3: *Positie van het SPP golfpakket langs een rechte geleider. De snelheid is lager dan dat van een foton in lucht en van een SPP op een vlakke film door de aanwezigheid van de geleider.*

figuur. In de frames 6.2(b) t/m 6.2(f) tonen we 5 opeenvolgende tijdframes van de amplitude van het propagerende SPP golfpakket van 120 fs. Tussen elk frame is de referentietak langer gemaakt met een lengte die overeen komt met 48 fs. Tot slot laten we in figuur 6.2(g) niet alleen de amplitude, maar ook de fase van het golfpakket zien. De individuele fasefronten zijn duidelijk zichtbaar als lijnen haaks op de geleider.

De groepssnelheid van dit SPP golfpakket bepalen we door het maximum van het pakket in de tijd te volgen zoals te zien is in figuur 6.3. De helling in de grafiek geeft een snelheid van $2.5 \cdot 10^8 \pm 0.3 \cdot 10^8$ m/s. De afstand tussen de fasefronten geeft ons de fasesnelheid, die $2.99 \cdot 10^8 \pm 0.01 \cdot 10^8$ m/s blijkt te zijn. Deze waarde ligt zeer dicht bij de fasesnelheid van licht in lucht en is gelijk aan berekeningen voor SPPs op een vlakke Au-film. Dezelfde berekeningen geven een groepssnelheid van $0.99 \cdot c$. De groepssnelheid is dus merkbaar verlaagd door de geleider.

Om de SPPs verder te vertragen fabriceerden we een SPP Bragg grating zoals getoond in figuur 6.4(a). Iedere "tand" van de grating reflecteert een klein beetje SPP E-veld. Voor een bepaald interval van golflengtes (de zogeheten "stopgap") interfereren alle reflecties destructief met de inkomende SPPs en wordt het voor het SPP onmogelijk om de grating binnen te gaan. Voor golflengtes in de buurt van

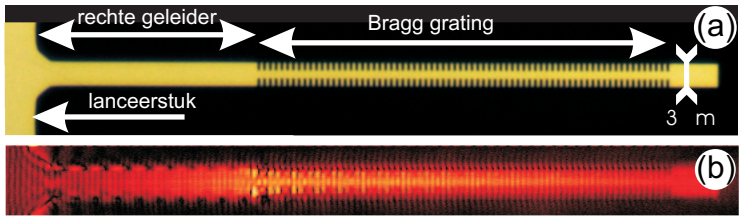

Figure 6.4: *(a): Langs de SPP geleider is een 55 mm lange Bragg grating gemaakt. SPPs komen van de linkerkant van de figuur en reizen via de rechte geleider naar de grating. Als ze over de grating propageren, doen ze dat met een snelheid van $c/2$, zoals te zien is in figuur 6.5. (b): Amplitude van het E-veld van het SPP, gemeten met de PSTM. Het is zichtbaar dat, in tegenstelling tot de amplitude in figuur 6.2(b) t/m (f), de amplitude in de grating gemodelleerd is. De rede hiervoor is dat de SPPs door de periodiciteit van de grating een zogeheten Bloch golf vormen [108].*

de "stopgap" is de dispersie erg groot en daalt de groepssnelheid. Een tijdsframe van een SPP golfpakket dat door de grating beweegt, is te zien in figuur 6.4(b). In het midden van de grating hielden we een 1 μm brede geleider vrij om er voor te zorgen dat de grating niet alle SPPs wegscatterd, maar dat het SPP door de grating wordt geleid. Op deze manier bereikt een groter deel van de langzame SPPs het einde van de grating. Het is goed te zien in de figuur dat het SPP ook vooral geconcentreerd is in de uitgespaarde geleider.

Zolang de SPPs zich nog in de rechte geleider bevinden, is de groepssnelheid ongeveer de lichtsnelheid: $3.1 \cdot 10^8 \pm 0.3 \cdot 10^8$ m/s (zie figuur 6.5). Eenmaal in de grating halveert de snelheid en wordt $1.5 \cdot 10^8 \pm 0.2 \cdot 10^8$ m/s. Dit experiment herhaalden we voor verschillende centrale golflengte van het golfpakket. Bij elke golflengte hebben we de groepsvertraging bepaald, dit is v_g/c, en een maat voor de vertraging van het SPP. De groepsvertraging voor verschillende golflengte is te zien in figuur 6.6. Onze grating blijkt een "stopgap" te hebben bij 1475 nm. Vlakbij de "stopgap" is de groepsvertraging maximaal, en enkele tientallen nm naast de "stopgap" is de invloed van de grating verdwenen.

Op het eerste gezicht lijkt een halvering van de groepssnelheid niet indrukwekkend. Voor fotonische kristallen zijn groepsvertragingen van boven de 1000 gemeten en met behulp van kwantum interferentie, in bijvoorbeeld een Bose-Einstein condensaat, kan licht zelfs helemaal worden stilgezet. Maar al deze grote vertragingsexperimenten gebruikten zeer beperkte bandbreedtes van GHz. of slechts MHz. De hier gemeten vertraging geldt voor de gehele bandbreedte van het SPP golfpakket van 30 nm, ofwel ordes van grootte meer dan voor kwantum interferentie. Als we kijken naar het product tussen bandbreedte en tijdsvertraging,

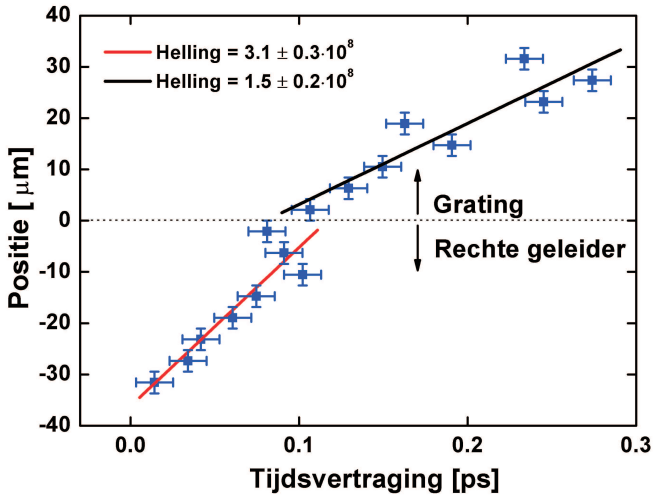

Figure 6.5: *De positie van de SPPs voor verschillende tijdsvertraging in zowel de rechte geleider als de grating. Het is duidelijk dat het SPP golfpakket tweemaal zo langzaam gaat als het door de grating moet.*

dé relevante parameter voor toepassingen, dan blijkt het gemeten langzame SPP het beste te scoren van alle alternatieven.

De factor twee vertraging vormt ook absoluut niet de bovengrens. Door een theoretisch model aan de groepsvertraging te fitten en de bandbreedte van het SPP golfpakket mee te nemen, komen we achter de mate van interactie tussen de SPPs en de grating. Berekenen we met deze interactie hoe langzaam een 10 ps golfpakket zou gaan, dan geeft dit een groepsvertraging van 100, zoals te zien is in figuur 6.6. Dit is een vertraging die toepassingen mogelijk maakt, helemaal omdat een bandbreedte van 10 ps goed is voor 100 GHz dataverwerking. Voor deze smallere bandbreedte blijft het product tussen de tijdsvertraging en bandbreedte uiteraard gelijk. Samen met nieuwe ontwikkelingen in de SPP propagatielengte [11], die nu al enkele millimeters kan zijn, opent deze vinding deuren naar plasmonische componenten voor in PC's.

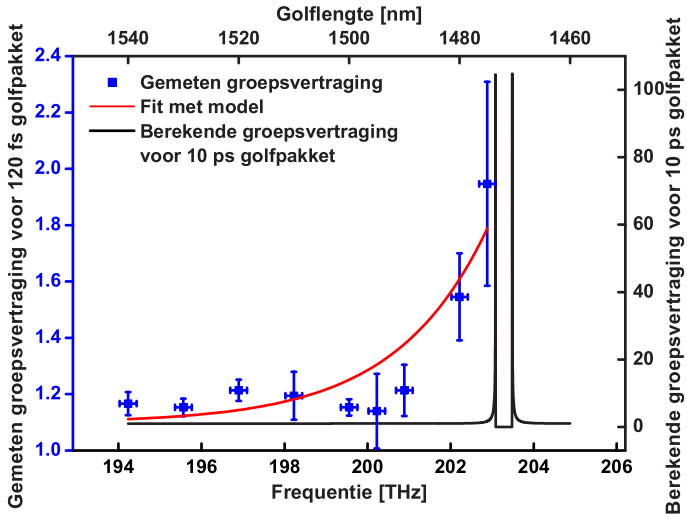

Figure 6.6: *De groepsvertraging v_g/c van het SPP blijkt afhankelijk van de frequentie. Direct naast de "stopgap" (1475 nm) is de vertraging het grootst en enkele nm verder is de invloed van de grating verdwenen. De rode lijn in de figuur is een fit met een model dat golven in een grating beschrijft en geeft de mate van interactie tussen de grating en het SPP. Voor een golfpakket van 10 ps in plaats van de 120 fs die wij gebruiken, voorspelt het model een groepsvertraging van 100.*

Dankwoord

"Gefeliciteerd! Ik moet er nu vandoor, maar binnenkort begin ik een nieuwe groep in Amsterdam en ik zou het leuk vinden als je daar komt promoveren."

Zo ongeveer begon vier en een half jaar geleden een avontuur dat nu is uitgemond in dit proefschrift. Kobus zat in mijn afstudeercommissie als extern lid en stond op het punt een eigen groep te beginnen op het AMOLF instituut. Blijkbaar had mijn afstudeeropdracht, over wat er gebeurt als je water of zand schudt, genoeg indruk gemaakt om mij te vragen of ik de eerste promovendus wilde worden in de nieuwe groep die helemaal niets met water en zand ging doen.

Ik wil Kobus bedanken voor het vertrouwen dat hij in mij had. Het is nogal een risico om iemand die nog nooit één stap een optisch lab had gezet, een opstelling te laten bouwen die zo complex is als de microscoop die er nu staat. Ook tijdens de lange frustrerende periode waarin de opstelling nèt niet goed genoeg werkte, bleef je altijd vertrouwen in een goede afloop. Dank voor die vele keren dat ik zwaar gefrustreerd bij jou kon uitrazen om vervolgens weer met frisse moed en nieuwe ideeën aan de slag te gaan. Ook wil ik je bedanken voor de vele minicolleges waarin je geduldig de basis van de optica uitlegde.

En daar sta je dan in een leeg lab. Twee tafels, dat was alles. Gelukkig was Hinco vanaf dag één altijd in de buurt voor hulp, advies, maar vooral ook voor een vrolijke noot.

Ik wil Jennifer en Janne bedanken voor de gastvrijheid en hulp om in hun lab mijn eerste stapjes in de wereld van lasers, spiegeltjes en lenzen te zetten. De Photonic Materials groep ben ik dankbaar dat ze me hebben opgenomen in hun groep zodat ik mij van het begin af aan op mijn plek voelde op het AMOLF.

Na driekwart jaar was hij daar dan eindelijk: mijn eerste groepsgenoot! Joris,

ik vond het een leuke ervaring om jou te mogen begeleiden en je was een leuke groepsgenoot. Gelukkig bleef het niet bij één. Rob E., je was er niet alleen voor vele stimulerende discussies, maar je was nog meer een kamergenoot met een zelfde soort gevoel voor humor, waardoor we om elke situatie ontzettend konden lachen, hoe ongepast dat soms ook was. Jord, ik heb er alle vertrouwen in dat het experiment dat ik altijd wilde doen, bij jou in goede handen is en mooie resultaten gaat opleveren. Thank you Matteo for your wise lessons on Italian food and cooking. I very much liked talking with you about physics, the Dutch, pasta etc. Nick en Olav, jullie waren er maar kort, maar toch leuk dat jullie onze groep hebben gekozen om af te studeren. Robert, je was meer een conferentiegenoot, dan een groepsgenoot omdat je in Twente zit. Maar als jij meeging op een conferentie wist je zeker dat het gezellig zou worden. Ik ben benieuwd of je snowboardervaring een vervolg krijgt.

PHANTOM was er nooit gekomen zonder de hulp van Henk, Idsart, Iliya, Rob K., Ton, en de hulp op afstand van Jeroen en Frans. Ook de werkplaats, voor het vakkundig fabriceren van onderdelen, en de huishoudelijke dienst, voor de stabiliteit in het lab, waren onmisbaar. Allemaal hartelijk dank voor de hulp. Hopelijk kunnen jullie samen met Marco K., Marco S. en Sjoerd PHANTOM tot de koplopers in de wereld behouden.

Chris en Ewold bedankt voor het leren werken in de cleanroom zodat ik mijn eigen samples daar kon maken.

Kamergenoten uit andere groepen zorgden voor een ander kijk op wetenschap en andere gesprekken, Dima en Otto, bedankt daarvoor.

Omdat er meer is dan wetenschap wil ik alle (oud) leden van de PV bedanken voor een gezellig tijd. Het uitje en de kerstlunch waren altijd evenementen om naar uit te kijken en ik heb het erg leuk gevonden om ze te helpen organiseren.

Ik wil alle leden van het Center for Nanophotonics bedanken voor een leerzame week op Ameland, de vele discussies tijdens de colloquia, maar vooral ook voor de gesprekken bij de koffie, de lunch en de vele overige gelegenheden binnen en buiten het AMOLF.

Bela, Ad en Rutger H. wil ik bedanken voor hun hulp bij de berekeningen in hoofdstuk 4. Dankzij jullie bijdrage kon ik de berekeningen doen die een absolute meerwaarde voor het hoofdstuk zijn.

Een aantal mensen wil ik nog bij naam noemen. Afric, jammer dat je zo snel naar Nijmegen verhuisde, je was een goede buur. Huub, bedankt dat je na een ongelukje in het lab zonder twijfelen in de auto stapte om mij naar het AMC te

brengen en je vrije avond opofferde om daar op mij te blijven wachten. Nicole, het was gezellig om samen met jou op en neer naar Haarlem te reizen en sorry dat er altijd vertraging is als ik met je meereis.

Tot slot wil ik mijn ouders, Martin, Sanja, Guido en Emiel en de rest van mijn familie, schoonfamilie en vrienden bedanken voor hun interesse in mijn onderzoek en steun de afgelopen vier jaar.
Marloes, bedankt voor je liefde. Of ik nu dolenthousiast was over de resultaten, of niet te genieten omdat de opstelling niet werkte, jij was er altijd voor me.

Marijn

References

[1] G. E. Moore, *Cramming more components onto integrated circuits*, Electronics **38** (1965).

[2] M. Schulz, *The end of the road for silicon?*, Science **399**, 229 (1999).

[3] M. J. Kobrinsky, B. A. Block, J.-F. Zheng, B. C. Barnett, E. Mohammed, M. Reshotko, F. Robertson, S. List, I. Young, and K. Cadien, *On-Chip Optical Interconnects*, Intel Technology Journal **8**, 129 (2004).

[4] J. D. Joannopoulos, P. R. Villeneuve, and S. Fan, *Photonic crystals: putting a new twist on light*, Nature **386**, 143 (1997).

[5] J. D. Joannopoulos, R. D. Meade, and J. N. Winn, *Photonic crystals: Modeling the flow of light*, Princeton University Press, Princeton NY, USA, 1995.

[6] W. L. Barnes, A. Dereux, and T. W. Ebbesen, *Surface plasmon subwavelength optics*, Nature **424**, 824 (2003).

[7] E. Ozbay, *Plasmonics: Merging Photonics and Electronics at Nanoscale Dimensions*, Science **311**, 189 (2003).

[8] H. Raether, *Surface Plasmons*, Springer-Verlag, Berlin, Germany, 1986.

[9] E. Kretschmann and H. Raether, *Radiative decay of nonradiative surface plasmons excited by light*, Z.Naturforsch. A **23**, 2135 (1968).

[10] J. Takahara, S. Yamagishi, H. Taki, A. Morimoto, and T. Kobayashi, *Guiding of a one-dimensional optical beam with nanometer diameter*, Optics Lett. **22**, 475 (1997).

[11] S. I. Bozhevolnyi, V. S. Volkov, E. Devaux, J.-Y. Laluet, and T. W. Ebbesen, *Channel plasmon subwavelength waveguide components including interferometers and ring resonators*, Nature **440**, 508 (2006).

[12] G. Gbur, H. F. Schouten, and T. D. Visser, *Achieving superresolution in near-field optical data readout systems using surface plasmons*, Appl. Phys. Lett. **87**, 191109 (2005).

[13] I. I. Smolyaninov, J. Elliott, A. V. Zayats, and C. C. Davis, *Far-Field Optical Microscopy with a Nanometer-Scale Resolution Based on the In-Plane Image Magnification by Surface Plasmon Polaritons*, Phys. Rev. Lett. **94**, 057401 (2005).

[14] D. Derkacs, S. H. Lim, P. Matheu, W. Mar, and E. T. Yu, *Improved performance of amorphous silicon solar cells via scattering from surface plasmon polaritons in nearby metallic nanoparticles*, Appl. Phys. Lett. **89**, 093103 (2006).

[15] W. D. Wilson, *Analyzing Biomelecular Interactions*, Science **295**, 2103 (2002).

[16] M. Soljačić and J. D. Joannopoulos, *Enhancement of nonlinear effects using photonic crystals*, Nature Materials **3**, 211 (2004).

[17] B. Hecht, H. Bielefeldt, L. Novotny, Y. Inouye, and D. W. Pohl, *Local Excitation,*

Scattering, and Interference of Surface Plasmons, Phys. Rev. Lett. **77**, 1889 (1996).

[18] H. Ditlbacher, J. R. Krenn, N. Felidj, B. Lamprecht, G. Schider, M. Salerno, A. Leitner, and F. R. Aussenegg, *Fluorescence imaging of surface plasmon fields*, Appl. Phys. Lett. **80**, 404 (2002).

[19] E. Verhagen, A. L. Tchebotareva, and A. Polman, *Erbium luminescence imaging of infrared surface plasmon polaritons*, Appl. Phys. Lett. **88**, 121121 (2006).

[20] A. Kubo, K. Onda, H. Petek, Z. Sun, Y. S. Jung, and H. K. Kim, *Femtosecond Imaging of Surface Plasmon Dynamics in a Nanostructured Silver Film*, Nano Lett. **5**, 1123 (2005).

[21] A. Kubo, N. Pontius, and H. Petek, *Femtosecond Microscopy of Surface Plasmon Polariton Wave Packet Evolution at the Silver/Vacuum Interface*, Nano Lett. **7**, 470 (2007).

[22] E. Betzig, J. K. Trautman, T. D. Harris, J. S. Weiner, and R. L. Kostelak, *Breaking the Diffraction Barrier: Optical Microscopy of a Nanometric Scale*, Science **251**, 1468 (1991).

[23] E. Betzig and J. K. Trautman, *Near-Field Optics: Microscopy, Spectroscopy, and Surface Modulation Beyond the Diffraction Limit*, Science **257**, 189 (1992).

[24] J.-C. Weeber, J. R. Krenn, A. Dereux, B. Lamprecht, Y. Lacroute, and J. P. Goudonnet, *Near-field observation of surface plasmon polariton propagation on thin metal stripes*, Phys. Rev. B **64**, 045411 (2001).

[25] R. Zia, J. A. Schuller, A. Chandran, and M. L. Brongersma, *Plasmonics: the next chip-scale technology*, Materials Today **9**, 20 (2006).

[26] M. Vaez-Iravani and R. Toledo-Crow, *Phase contrast and amplitude pseudo-heterodyne interference near field scanning optical microscopy*, Appl. Phys. Lett. **62**, 1044 (1993).

[27] M. L. M. Balistreri, J. P. Korterik, L. Kuipers, and N. F. van Hulst, *Local Observations of Phase Singularities in Optical Fields in Waveguide Structures*, Phys. Rev. Lett. **85**, 294 (2000).

[28] R. Hillenbrand and F. Keilmann, *Complex Optical Constants on a Subwavelength Scale*, Phys. Rev. Lett. **85**, 3029 (2000).

[29] A. Nesci, R. Dändliker, and H. P. Herzig, *Quantitative amplitude and phase measurement by use of a heterodyne scanning near-field optical microscope*, Optics Lett. **26**, 208 (2001).

[30] M. L. M. Balistreri, H. Gersen, J. P. Korterik, L. Kuipers, and N. F. van Hulst, *Tracking Femtosecond Laser Pulses in Space and Time*, Science **295**, 1080 (2001).

[31] A. Nesci and Y. Fainman, *Complex amplitude of an ultra-short pulse with femtosecond resolution in a waveguide using a coherent NSOM at 1550 nm*, in *48th SPIE Annual Meeting Symposium, SPIE Proc.*, San Diego, USA, page 6269,

2003.

[32] I. Stefanon, S. Blaize, A. Bruyant, S. Aubert, G. Lerondel, R. Bachelot, and P. Royer, *Heterodyne detection of guided waves using a scattering-type Scanning Near-Field Optical Microscope*, Optics Express **13**, 5553 (2005).

[33] I. I. Smolyaninov, W. Atia, and C. C. Davis, *Near-field optical microscopy of two-dimensional photonic and plasmonic crystals*, Phys. Rev. B **59**, 2454 (1999).

[34] S. I. Bozhevolnyi, J. Erland, K. Leosson, P. M. W. Skovgaard, and J. M. Hvam, *Waveguiding in Surface Plasmon Polariton Band Gap Structures*, Phys. Rev. Lett. **86**, 3008 (2001).

[35] J.-C. Weeber, Y. Lacroute, and A. Dereux, *Optical near-field distributions of surface plasmon waveguide modes*, Phys. Rev. B **68**, 115401 (2003).

[36] R. Zia, J. A. Schuller, and M. L. Brongersma, *Near-field characterization of guided polariton propagation and cutoff in surface plasmon waveguides*, Phys. Rev. B **74**, 165415 (2006).

[37] H. L. Offerhaus, B. van den Bergen, M. Escalante, F. B. Segerink, J. P. Korterik, and N. F. van Hulst, *Creating Focused Plasmons by Noncollinear Phasematching on Functional Gratings*, Nano Lett. **5**, 2144 (2005).

[38] A. D. McFarland and R. P. V. Duyne, *Single Silver Nanoparticles as Real-Time Optical Sensors with Zeptomole Sensitivity*, Nano Lett. **3**, 1057 (2003).

[39] J. Homola, *Present and future of surface plasmon resonance biosensors*, Anal. Bioanal. Chem. **377**, 528 (2003).

[40] H. H. Rotermund, *Imaging of dynamic processes on surfaces by light*, Surf. Sci. Rep. **29**, 267 (1997).

[41] M. van Exter and A. Lagendijk, *Ultra-short Surface plasmon and phonon dynamics*, Phys. Rev. Lett. **60**, 49 (1988).

[42] J. A. Veerman, A. M. Otter, L. Kuipers, and N. F. van Hulst, *High definition aperture probes for near-field optical microscopy fabricated by focused ion beam milling*, Appl. Phys. Lett. **72**, 3115 (1998).

[43] E. Betzig, P. L. Finn, and J. S. Weiner, *Combined shear force and near-field scanning optical microscopy*, Appl. Phys. Lett. **60**, 2484 (1992).

[44] K. Karrai and R. D. Grober, *Piezoelectric tip-sample distance control for near field optical microscopes*, Appl. Phys. Lett. **66**, 1842 (1995).

[45] C. L. Jahncke, O. Brandt, K. E. Fellows, and H. D. Hallen, *Choosing a preamplifier for tuning fork signal detection in scanning force microscopy*, Rev. Sci. Instrum. **75**, 2759 (2004).

[46] A. G. T. Ruiter, J. A. Veerman, K. O. van der Werf, and N. F. van Hulst, *Dynamic behavior of tuning fork shear-force feedback*, Appl. Phys. Lett. **71**, 28 (1997).

[47] H. Gersen, J. P. Korterik, N. F. van Hulst, and L. Kuipers, *Tracking ultrashort pulses through dispersive media: Experiment and theory*, Phys. Rev. E **68**, 026604 (2003).

[48] R. J. P. Engelen, Y. Sugimoto, Y. Watanabe, J. P. Korterik, N. Ikeda, N. F. van Hulst, K. Asakawa, and L. Kuipers, *The effect of higher-order dispersion on slow light propagation in photonic crystal waveguides*, Optics Express **14**, 1658 (2006).

[49] R. Zia, M. D. Selker, and M. L. Brongersma, *Leaky and bound modes of surface plasmon waveguides*, Phys. Rev. B **71**, 165431 (2005).

[50] G. A. Wurtz, R. Pollard, and A. V. Zayats, *Optical Bistability in Nonlinear Surface-Plasmon Polaritonic Crystals*, Phys. Rev. Lett. **97**, 057402 (2006).

[51] S. Jetté-Charbonneau, R. Charbonneau, N. Lahoud, G. Mattiussi, and P. Berini, *Demonstration of Bragg gratings based on long-ranging surface plasmon polariton waveguides*, Opt. Express **13**, 4674 (2005).

[52] J.-C. Weeber, Y. Lacroute, A. Dereux, E. Devaux, T. Ebbesen, C. Girard, M. U. Gonzalez, and A.-L. Baudrion, *Near-field characterization of Bragg mirrors engraved in surface plasmon waveguides*, Phys. Rev. B. **70**, 235406 (2004).

[53] L. Poladian, *Group-delay reconstructionfor fiber Bragg gratings in reflection and transmission*, Optics Lett. **22**, 1571 (1997).

[54] A. Bruyant, G. Lerondel, S. Blaize, I. Stefanon, S. Aubert, R. Bachelot, and P. Royer, *Local complex reflectivity in optical waveguides*, Phys. Rev. B **74**, 075414 (2006).

[55] H. Gersen, T. J. Karle, R. J. P. Engelen, W. Bogaerts, J. P. Korterik, N. F. van Hulst, T. F. Krauss, and L. Kuipers, *Direct Observation of Bloch Harmonics and Negative Phase Velocity in Photonic Crystal Waveguides*, Phys. Rev. Lett. **94**, 123901 (2005).

[56] D. M. Profunser, O. B. Wright, and O. Matsuda, *Imaging Ripples on Phononic Crystals Reveals Acoustic Band Structure and Bloch Harmonics*, Phys. Rev. Lett. **97** (2006).

[57] F. Bloch, *Über die Quantenmechanik der Elektronen in Kristallgittern*, Z. Physik **52**, 555 (1928).

[58] L. A. Weller-Brophy and D. G. Hall, *Analysis of waveguide gratings: application of Rouard's method*, J. Opt. Soc. Am. A **2**, 863 (1985).

[59] P. St. J. Russell, *Optics of Floquet-Bloch Waves in Dielectric Gratings*, Appl. Phys. B **39**, 231 (1986).

[60] C. Kittel, *Introduction to Solid State Physics*, Wiley, New York, USA, 1996.

[61] Y. Sugawara, O. B. Wright, and O. Matsuda, *Direct access to the dispersion relations of multiple anisotropic surface acoustic modes by Fourier image analysis*, Appl. Phys. Lett. **83**, 1340 (2003).

[62] A. A. Sukhorukov, D. Neshev, W. Krolikowski, and Y. S. Kivshar, *Nonlinear Bloch-Wave Interaction and Bragg Scattering in Optically Induced Lattices*, Phys. Rev. Lett. **92**, 093901 (2004).

[63] D. Gérard, L. Salomon, F. de Fornel, and A. Zayats, *Analysis of the Bloch mode spectra of surface polaritonic crystals in the weak and strong coupling regimes: grating-enhanced transmission at oblique incidence and suppression of SPP radiative losses*, Optics Express **12**, 3652 (2004).

[64] M. Lončar, D. Nedeljković, T. P. Pearsall, J. Vučković, A. Scherer, S. Kuchinsky, and D. C. Allan, *Experimental and theoretical confirmation of Bloch-mode light propagation in planar photonic crystal waveguides*, Appl. Phys. Lett. **80**, 1689 (2002).

[65] M. Martin, T. Benyattou, R. Orobtchouk, A. Talneau, A. Berrier, M. Mulot, and S. Anand, *Evidence of Bloch wave propagation within photonic crystal waveguides*, Appl. Phys. B **82**, 9 (2006).

[66] S. I. Bozhevolnyi and L. Kuipers, *Near-field characterization of photonic crystal waveguides*, Semicond. Sci. Technol. **21**, R1 (2006).

[67] S. I. Bozhevolnyi, B. Vohnsen, and E. A. Bozhevolnaya, *Transfer functions in collection scanning near-field optical microscopy*, Optics Comm. **172**, 171 (1999).

[68] B. Hecht, H. Bielefeldt, Y. Inouye, D. W. Pohl, and L. Novotny, *Facts and artifacts in near-field optical microscopy*, J. Appl. Phys. **81**, 2465 (1997).

[69] R. H. Ritchie, *Plasma Losses by Fast Electrons in Thin Films*, Phys. Rev. **106**, 874 (1957).

[70] D. Gauthier, *Slow light brings faster communications*, Physics World **12**, 30 (2005).

[71] T. J. Mok and B. J. Eggleton, *Expect more delays*, Nature **433**, 811 (2005).

[72] L. V. Hau, H. S. E., Z. Dutton, and C. H. Behroozi, *Light speed reduction to 17 meters per second in an ultra cold atomic gas*, Nature **397**, 594 (1999).

[73] M. D. Lukin and A. Imamoğlu, *Controlling photons using electromagnetically induced transparency*, Nature **412**, 273 (2001).

[74] A. V. Turukhin, V. S. Sudarshanam, M. S. Shahriar, J. A. Musser, B. S. Ham, and P. R. Hemmer, *Observation of Ultraslow and Stored Light Pulses in a Solid*, Phys. Rev. Lett. **88**, 023602 (2001).

[75] M. S. Bigelow, N. N. Lepeshkin, and R. W. Boyd, *Superluminal and Slow Light Propagation in a Room-Temperature Solid*, Nature **301**, 200 (2003).

[76] M. Bajcsy, A. S. Zibrov, and M. D. Lukin, *Stationary pulses of light in an atomic medium*, Nature **426**, 638 (2003).

[77] P.-C. Ku, F. Sedgwick, C. J. Chang-Hasnain, P. Palinginis, T. Li, H. Wang, S.-W. Chang, and S.-L. Chuang, *Slow light in semiconductor quantum wells*, Opt. Lett.

29, 2291 (2004).

[78] C. M. Soukoulis, *Photonic Crystals and Light Localization in the 21st Century*, NATO Science Series, Kluwer Academic, Dordrecht, The Netherlands, 2001.

[79] H. Gersen, T. J. Karle, R. J. P. Engelen, W. Bogaerts, J. P. Korterik, N. F. van Hulst, T. F. Krauss, and L. Kuipers, *Real-Space Observation of Ultraslow Light in Photonic Crystal Waveguides*, Phys. Rev. Lett. **94**, 073903 (2005).

[80] Y. A. Vlasov, M. OBoyle, H. F. Hamann, and S. J. McNab, *Active control of slow light on a chip with photonic crystal waveguides*, Nature **438**, 65 (2005).

[81] Y. Okawachi, M. S. Bigelow, J. E. Sharping, Z. Zhu, A. Schweinsberg, D. J. Gauthier, R. W. Boyd, and A. L. Gaeta, *Tunable All-Optical Delays via Brillouin Slow Light in an Optical Fiber*, Phys. Rev. Lett. **94**, 153902 (2005).

[82] Y. Okawachi, M. Foster, J. Sharping, A. Gaeta, Q. Xu, and M. Lipson, *All-optical slow-light on a photonic chip*, Optics Express **14**, 2317 (2006).

[83] J. G. Rivas, M. Kuttge, P. H. Bolivar, H. Kurz, and J. A. Sanchez-Gil, *Propagation of Surface Plasmon Polaritons on Semiconductor Gratings*, Phys. Rev. Lett. **93**, 256804 (2004).

[84] Y. Fainman, *Nanophotonics for Information Systems Integration*, in *OSA Topical Meetings on Integrated Photoncs Resaerch and Applications*, Uncasville, Connecticut, USA, 2006.

[85] P. St. J. Russel, *Bloch wave analysis of dispersion and pulse propagation in pure distributed feedback structures*, J. Mod. Optics **38**, 1599 (1991).

[86] F. Yang, J. R. Sambles, and G. W. Bradberry, *Long-range surface modes supported by thin films*, Phys. Rev. B **44**, 5855 (1991).

[87] M. Quinten, A. Leitner, J. R. Krenn, and F. R. Aussenegg, *Electromagnetic energytransport via linear chains of silver nanoparticles*, Optics Lett. **23**, 1331 (1998).

[88] S. A. Maier, P. G. Kik, H. A. Atwater, S. Meltzer, E. Harel, B. E. Koel, and A. A. G. Requicha, *Local detection of electromagnetic energy transport below the diffraction limit in metal nanoparticle plasmon waveguides*, Nature Materials **2**, 229 (2003).

[89] T. Nikolajsen, K. Leosson, and S. I. Bozhevolnyi, *Surface plasmon polariton based modulators and switches operating at telecom wavelengths*, Appl. Phys. Lett. **85**, 5833 (2004).

[90] H. M. Gibbs, *Optical Bistability: Controlling Light with Light*, Academic, New York, USA, 1985.

[91] T. W. Ebbesen, H. J. Lezec, T. Thio, and P. A. Wolff, *Extraordinary optical transmission through sub-wavelength hole arrays*, Nature **391**, 667 (1998).

[92] K. J. Klein Koerkamp, S. Enoch, F. B. Segerink, N. F. van Hulst, and L. Kuipers,

Strong Influence of Hole Shape on Extraordinary Transmission through Periodic Arrays of Subwavelength Holes, Phys. Rev. Lett. **92**, 183901 (2004).

[93] K. L. van der Molen, K. J. Klein Koerkamp, S. Enoch, S. F. B., van Hulst N. F., and L. Kuipers, *Role of shape and localized resonances in extraordinary transmission through periodic arrays of subwavelength holes: Experiment and theory*, Phys. Rev. B **72**, 045421 (2005).

[94] Y. Liu, J. Bishop, L. Williams, S. Blair, and J. Herron, *Biosensing based upon molecular confinement in metallic nanocavity arrays*, Nanotechnology **15**, 1368 (2004).

[95] J. A. H. van Nieuwstadt, M. Sandtke, R. H. Harmsen, F. B. Segerink, J. C. Prangsma, S. Enoch, and L. Kuipers, *Strong Modification of the Nonlinear Optical Response of Metallic Subwavelength Hole Arrays*, Phys. Rev. Lett. **97**, 146102 (2006).

[96] R. Rokitski, K. A. Tetz, and Y. Fainman, *Propagation of Femtosecond Surface Plasmon Polariton Pulses on the Surface of a Nanostructured Metallic Film: Space-Time Complex Amplitude Characterization*, Phys. Rev. Lett. **95**, 177401 (2005).

[97] H. F. Schouten, T. D. Visser, D. Lenstra, and H. Blok, *Light transmission through a subwavelength slit: Waveguiding and optical vortices*, Phys. Rev. E **67**, 036608 (2003).

[98] H. Fischer, A. Nesci, G. Lévêque, N. Janunts, and O. J. Martin, *Correlation between phase singularities and enhanced optical transmission in subwavelength apertures*, in *Nanometa, First European Topical Meeting on Nanophotonics and Metamaterials*, Seefeld, Austria, 2007.

[99] R. A. Shelby, D. R. Smith, and S. Schultz, *Experimental verification of a negative index of refraction*, Science **292**, 77 (2001).

[100] G. Dolling, C. Enkrich, M. Wegener, C. M. Soukoulis, and S. Linden, *Simultaneous Negative Phase and Group Velocity of Light in a Metamaterial*, Science **312**, 892 (2006).

[101] V. G. Veselago, *The electrodynamics of substances with simultaneously negative values of ϵ and μ*, Sov. Phys. Usp. **10**, 509 (1968).

[102] J. B. Pendry, *Negative Refraction Makes a Perfect Lens*, Phys. Rev. Lett. **85**, 3966 (2000).

[103] N. Fang, H. Lee, C. Sun, and X. Zhang, *SubDiffraction-Limited Optical Imaging with a Silver Superlens*, Science **308**, 534 (2005).

[104] Z. Liu, H. Lee, Y. Xiong, C. Sun, and X. Zhang, *Far-Field Optical Hyperlens Magnifying Sub-Diffraction-Limited Objects*, Science **315**, 1686 (2007).

[105] I. I. Smolyaninov, Y.-J. Hung, and C. C. Davis, *Magnifying Superlens in the Visible Frequency Range*, Science **315**, 1699 (2007).

[106] J. B. Pendry, D. Schurig, and D. R. Smith, *Controlling Electromagnetic Fields*, Science **312**, 1780 (2006).

[107] D. Schurig, J. J. Mock, B. J. Justice, S. A. Cummer, J. B. Pendry, A. F. Starr, and D. R. Smith, *Metamaterial Electromagnetic Cloak at Microwave Frequencies*, Science **314**, 977 (2006).

[108] N. W. Ashcroft and N. D. Mermin, *Solid state physics*, Thomson Learning, USA, 1976.